TOPICAL REVIEW

Wide bandgap GaN-based semiconductors for spintronics

S J Pearton[1]**, C R Abernathy**[1]**, G T Thaler**[1]**, R M Frazier**[1]**, D P Norton**[1]**,
F Ren**[2]**, Y D Park**[3]**, J M Zavada**[4]**, I A Buyanova**[5]**, W M Chen**[5]
and A F Hebard[6]

[1] Department of Materials Science and Engineering, University of Florida, Gainesville,
FL 32611, USA
[2] Department of Chemical Engineering, University of Florida, Gainesville, FL 32611, USA
[3] CSCMR and School of Physics, Seoul National University, Seoul 151-747, Korea
[4] US Army Research Office, Research Triangle Park, NC 27709, USA
[5] Department of Physics and Measurement Technology, Linköping University,
S-581 83 Linköping, Sweden
[6] Department of Physics, University of Florida, Gainesville, FL 32611, USA

Abstract
Recent results on achieving ferromagnetism in transition-metal-doped GaN,
AlN and related materials are discussed. The field of semiconductor spintronics
seeks to exploit the spin of charge carriers in new generations of transistors,
lasers and integrated magnetic sensors. There is strong potential for new classes
of ultra-low-power, high speed memory, logic and photonic devices based on
spintronics. The utility of such devices depends on the availability of materials
with practical magnetic ordering temperatures and most theories predict that the
Curie temperature will be a strong function of bandgap. We discuss the current
state-of-the-art in producing room temperature ferromagnetism in GaN-based
materials, the origins of the magnetism and its potential applications.

(Some figures in this article are in colour only in the electronic version)

Contents

1. Introduction

There is great current interest in the emerging field of semiconductor spin transfer electronics (spintronics), which seeks to exploit the spin of charge carriers in semiconductors. It is widely expected that new functionalities for electronics and photonics can be derived if the injection, transfer and detection of carrier spin can be controlled above room temperature. Among this new class of devices are magnetic devices with gain, spin transistors operating at very low powers for mobile applications that rely on batteries, optical emitters with encoded information through their polarized light output, fast non-volatile semiconductor memory and integrated magnetic/electronic/photonic devices ('electromagnetism-on-a-chip'). Since the magnetic properties of ferromagnetic semiconductors are a function of carrier concentration in the material in many cases, then it will be possible to have electrically or optically controlled magnetism through field-gating of transistor structures or optical excitation to alter the carrier density. A number of recent reviews have covered the topics of spin injection, coherence length and magnetic properties of materials systems such as in the general areas of spin injection from metals into semiconductors and applications of the spintronic phenomena [1–4]. Although there have been recent reports of successful and efficient spin injection from a metal to a semiconductor even at room temperature by ballistic transport (i.e. Schottky barriers and tunnelling), the realization of functional spintronic devices may well require materials with ferromagnetic ordering at operational temperatures compatible with existing semiconductor materials. To realize semiconductor spintronic devices one can inject polarized carriers from a ferromagnetic metal into either a non-ferromagnetic or dilute magnetic semiconductor, or alternatively use a ferromagnetic semiconductor as the active region or injector. The latter has advantages in terms of having more compatible interfaces and avoiding conductivity mismatch. In this review we focus on materials for this second approach.

2. Potential semiconductor materials for spintronics

There are two major criteria for selecting the most promising materials for semiconductor spintronics. First, the ferromagnetism should be retained to practical temperatures (i.e. >300 K) [5–8]. Second, it would be a major advantage if there were already an existing technology base for the material in other applications. Most of the work in the past has focused on (Ga, Mn)As and (In, Mn)As. There are indeed major markets for their host materials in infrared light-emitting diodes and lasers and high speed digital electronics (GaAs) and magnetic sensors (InAs). In single-phase samples carefully grown by molecular beam epitaxy (MBE), the highest Curie temperatures reported are $\sim$110 K for (Ga, Mn)As and $\sim$35 K for (In, Mn)As as one of the most effective methods for investigating spin-polarized transport is by monitoring the polarized electroluminescence output from a quantum-well light-emitting diode into which the spin current is injected. Quantum selection rules relating the initial carrier spin polarization and the subsequent polarized optical output can provide a quantitative measure of the injection efficiency.

There are a number of essential requirements for achieving practical spintronic devices in addition to the efficient electrical injection of spin-polarized carriers. These include the ability to transport the carriers with high transmission efficiency within the host semiconductor or conducting oxide, the ability to detect or collect the spin-polarized carriers and to be able to control the transport through external means such as biasing of a gate contact on a transistor structure.

We focus on a particular and emerging aspect of spintronics, namely recent developments in achieving practical magnetic ordering temperatures in technologically useful semiconductors [5–10]. While the progress in synthesizing and controlling the magnetic properties of III-arsenide semiconductors has been astounding, the reported Curie temperatures are too low to have any significant practical impact.

Other materials for which room temperature ferromagnetism has been reported include $(Cd, Mn)GeP_2$ [6], $(Zn, Mn)GeP_2$ [7], $ZnSnAs_2$ [8], $(Zn, Co)O$ [9] and $(Co, Ti)O_2$ [10]. Some of these chalcopyrites and wide bandgap oxides have interesting optical properties, but they lack a technology and experience base as large as that of most semiconductors.

The key breakthrough that focused attention on wide bandgap semiconductors as being the most promising for achieving practical ordering temperatures was the theoretical work of Dietl $et\ al$ [11]. They predicted that cubic GaN doped with $\sim$5 at.% of Mn and containing a high concentration of holes (3.5×10^{20} cm^{-3}) should exhibit a Curie temperature exceeding room temperature. In the period following the appearance of this work, there has been tremendous progress on both the realization of high-quality (Ga, Mn)N epitaxial layers and on the theory of ferromagnetism in these so-called dilute magnetic semiconductors (DMS). The term 'DMS' refers to the fact that some fraction of the atoms in a non-magnetic semiconductor like GaN are replaced by magnetic ions. A key, unanswered question is whether the resulting material is indeed an alloy of (Ga, Mn)N or whether it remains as GaN with clusters, precipitates or second phases that are responsible for the observed magnetic properties [12].

3. Mechanisms of ferromagnetism

Two basic approaches to understanding the magnetic properties of dilute magnetic semiconductors have emerged. The first class of approaches is based on mean-field theory. The theories that fall into this general model implicitly assume that the dilute magnetic semiconductor is a more-or-less random alloy, e.g. (Ga, Mn)N, in which Mn substitutes for one of the lattice constituents. The second class of approaches suggests that the magnetic atoms form small (a few atoms) clusters that produce the observed ferromagnetism [12]. A difficulty in experimentally verifying the mechanism responsible for the observed magnetic properties is that, depending on the growth conditions employed for growing the DMS material, it is likely that one could readily produce samples that span the entire spectrum of possibilities from single-phase random alloys to nanoclusters of the magnetic atoms to precipitates and second-phase formation. Therefore, it is necessary to decide on a case-by-case basis which mechanism is applicable. This can only be achieved by a careful correlation of the measured magnetic properties with materials analysis methods that are capable of detecting other phases or precipitates. If, for example, the magnetic behaviour of the DMS is characteristic of that of a known ferromagnetic second phase (such as MnGa or Mn_4N in (Ga, Mn)N), then clearly the mean-field models are not applicable. To date, most experimental reports concerning room temperature ferromagnetism in DMS employ x-ray diffraction, selected-area diffraction patterns, transmission electron microscopy, photoemission or x-ray absorption (including extended x-ray absorption fine structure, EXAFS, as discussed later) to determine whether
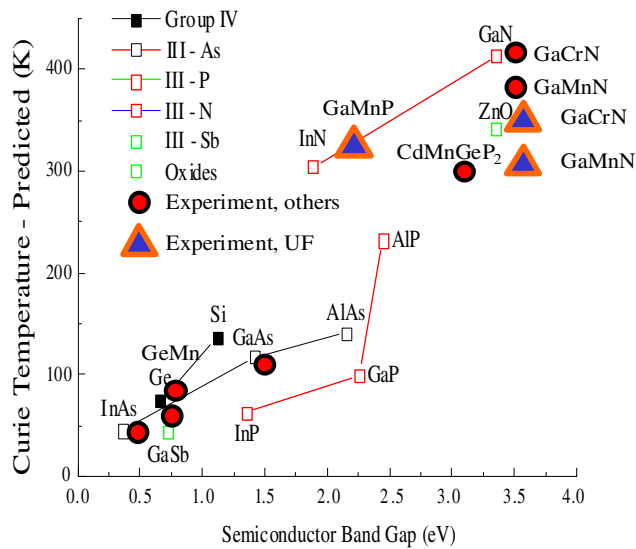
Figure 1. Predicted Curie temperatures as a function of bandgap, along with some experimental results.

the magnetic atoms are substituting for one of the lattice constituents to form an alloy. Given the level of dilution of the magnetic atoms, it is often very difficult to categorically determine the origin of the ferromagnetism. Indirect means, such as superconducting quantum interference device (SQUID) magnetometer measurements, to exclude any ferromagnetic inter-metallic compounds as the source of magnetic signals and even the presence of what is called the anomalous or extraordinary Hall effect, that have been widely used to verify a single-phase system, may be by itself insufficient to characterize a DMS material.

The mean-field approach basically assumes that the ferromagnetism occurs through interactions between the local moments of the Mn atoms, which are mediated by free holes in the material. The spin–spin coupling is also assumed to be a long-range interaction, allowing use of a mean-field approximation [13–20]. In its basic form, this model employs a virtual-crystal approximation to calculate the effective spin density due to the Mn ion distribution. The direct Mn–Mn interactions are antiferromagnetic so that the Curie temperature, T_C, for a given material with a specific Mn concentration and hole density (derived from Mn acceptors and/or intentional shallow level acceptor doping) is determined by competition between the ferromagnetic and anti-ferromagnetic interactions. Numerous refinements of this approach have appeared recently, taking into account the effects of positional disorder [16, 17], indirect exchange interactions [18], spatial inhomogeneities and free-carrier spin polarization [19, 20]. Figure 1 shows a compilation of the predicted T_C values, together with some experimental results. In the subsequent period after appearance of the Dietl *et al* [11] paper, remarkable progress has been made on the realization of materials with T_C values at or above room temperature. While most of the theoretical work for DMS materials has focused on the use of Mn as the magnetic dopant, there has also been some progress on identifying other transition metal atoms that may be effective. Figure 2 summarizes the two main theoretical approaches to understanding the ferromagnetism. In the mean-field theories, the Mn ions are considered to be embedded in a high concentration of free carriers that mediate the coupling between the Mn ions. In the bound magnetic polaron (BMP) models, the carrier concentration is much less than the Mn density and BMPs form consisting of carriers localized around large clusters
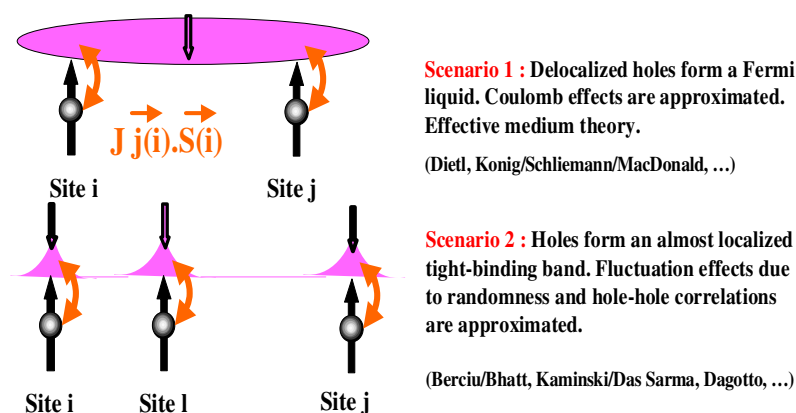
Scenario 1 : Delocalized holes form a Fermi liquid. Coulomb effects are approximated. Effective medium theory.

(Dietl, Konig/Schliemann/MacDonald, ...)

Scenario 2 : Holes form an almost localized tight-binding band. Fluctuation effects due to randomness and hole-hole correlations are approximated.

(Berciu/Bhatt, Kaminski/Das Sarma, Dagotto, ...)

Figure 2. Schematic of theoretical approaches for ferromagnetism mechanisms in dilute magnetic semiconductors. The top figure represents the mean field approach and the bottom the bound magnetic polaron approach.

of Mn. As the temperature is lowered, the diameter of the BMPs increases and eventually overlaps at the Curie temperature.

3.1. (Ga, Mn)N

In epitaxial GaN layers grown on sapphire substrates and then subjected to solid state diffusion of Mn at temperatures from 250 to 800 °C for various periods, clear signatures of room temperature ferromagnetism were observed [21, 22]. An anomalous Hall effect was observed at 323 K. The Curie temperature was found to be in the range 220–370 K, depending on the diffusion conditions. The use of ion implantation to introduce the Mn produced lower magnetic ordering temperatures [23, 24].

In initial work from Japan, (Ga, Mn)N films grown by MBE at temperatures between 580 and 720 °C with Mn contents of 6–9 at.%, magnetization (M) versus magnetic field (H) curves showed clear hysteresis at 300 K, with coercivities of 52–85 Oe and residual magnetizations of 0.08–0.77 emu g^{-1} at this temperature. An estimated T_C of 940 K was reported, using a mean-field approximation to analyse the experimental data [25]. Note that, while the electrical properties of the samples were not measured, they were almost certainly n-type [26–28]. As we discussed above, it is difficult to obtain high Curie temperatures in n-type DMS materials according to the mean-field theories and this is something that needs to be addressed in future refinements of these theories. The 940 K result is now considered to be most likely due to MnGa or Mn$_4$N inclusions and not to single-phase (Ga, Mn)N.

Room temperature ferromagnetism in single-phase n-type (Ga, Mn)N grown by MBE has also been reported by our group [29], as shown in figure 3. In general, no second phases are found for Mn levels below ∼10% for growth temperatures of ∼750 °C. The (Ga, Mn)N retains n-type conductivity under these conditions. In that case, strenuous efforts were made to exclude any possible contribution from the sample holder in the SQUID magnetometer or other spurious effects. It is also worthwhile pointing out that, for the studies of (Ga, Mn)N showing ferromagnetic ordering by magnetization measurements, a number of materials characterization techniques did not show the presence of any second ferromagnetic phases within detectable limits. In addition, the values of the measured coercivities are relatively small. If indeed there were undetectable amounts of nano-sized clusters, due to geometrical effects, the
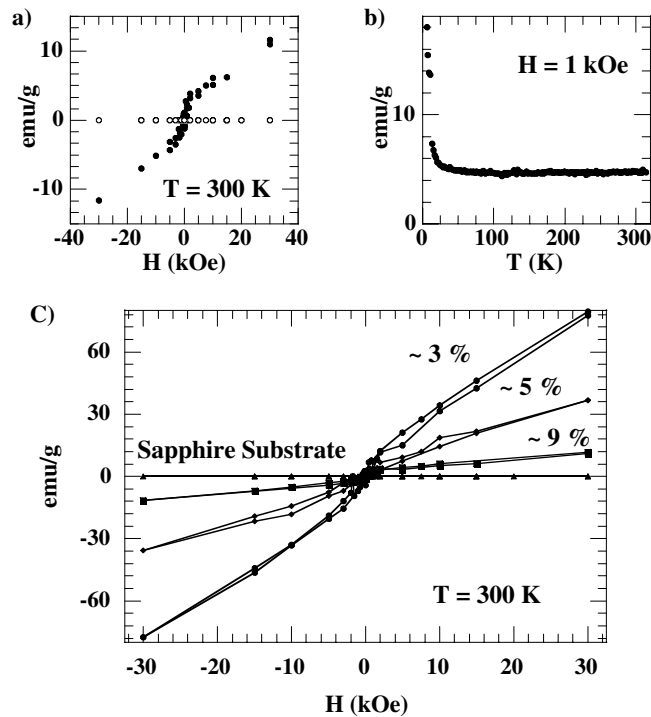
a)

b)

C)

Figure 3. (a) $B-H$ from MBE-grown (Ga, Mn)N with 9.4 at.% Mn (full circles) and from sapphire substrate (open circles), (b) $M-T$ of (Ga, Mn)N, (c) $B-H$ from (Ga, Mn)N as a function of Mn concentration.

expected fields at which these clusters would switch magnetically would be expected to be much larger than what has been observed. In accordance with most of the theoretical predictions, magnetotransport data showed the anomalous Hall effect, negative magnetoresistance and magnetic resistance at temperatures that were dependent on the Mn concentration. For example, in films with very low (<1%) or very high (~9%) Mn concentrations, the Curie temperatures were between 10 and 25 K. An example is shown in figure 3 for an n-type (Ga, Mn)N sample with Mn ~7%. The sheet resistance shows negative magnetoresistance below 150 K, with the anomalous Hall coefficient disappearing below 25 K. When the Mn concentration was decreased to 3 at.%, the (Ga, Mn)N showed the highest degree of ordering per Mn atom. Figure 3(a) shows hysteresis present at 300 K, while the magnetization as a function of temperature is shown in figure 3(b). Data from samples with different Mn concentrations are shown in figure 3(c) and indicate ferromagnetic coupling, leading to a lower moment per Mn. Data from field-cooled and zero-field-cooled conditions were further suggestive of room temperature magnetization. The significance of these results is that there are many advantages from a device viewpoint to having n-type ferromagnetic semiconductors. Extended x-ray absorption fine structure (EXAFS) measurements have been performed on (Ga, Mn)N samples grown by a group in Japan using MBE on sapphire at temperatures of 400–650 °C with Mn concentrations of $\sim 7 \times 10^{20}$ cm^{-3} (i.e. slightly over 2 at.%) [30]. Most of the Mn substituted for Ga on substitutional lattice positions. In the samples grown at 650 °C, <1 at.% of the total amount of Mn was found to be present as Mn clusters. However at lower growth temperatures (400 °C), the amount of Mn that could be present as clusters increased

up to ∼36 at.% of the total Mn incorporated. The ionic state of the substitutional Mn was found to be primarily Mn(2), so that these impurities act as acceptors when substituting for the Ga with valence 3. However, when the electrical properties of these samples were measured, they were found to be resistive [29]. This result emphasizes how much more needs to be understood concerning the effects of compensation and unintentional doping of (Ga, Mn)N, since the EXAFS data indicated the samples should have shown very high p-type conductivity due to the incorporation of Mn acceptors.

However, there are still strong variations in the reported magnetic behaviour, with some films exhibiting only paramagnetism and even those with ferromagnetism showing a wide range of apparent Curie temperatures (T_C) [31–40]. In particular, the origin of this ferromagnetism is not clear. Current hypotheses include a mean-field model (based on the Ruderman–Kittel–Kasuya–Yoshida (RKKY) interaction) in which the ferromagnetism results from carrier mediation by delocalized or weakly localized holes in p-type material or various types of small clusters of Mn such as Mn_xN. Given that the $Mn^{3+/2+}$ acceptor level is deep ($\sim E_V + 1.8$ eV), it is not expected that free-carrier-mediated magnetism is significant but tightly bound carriers could play a role. The first class of approaches is based on mean-field theory which originates in the original model of Zener magnetism [41–43]. The theories that fall into this general model implicitly assume that the dilute magnetic semiconductor is a more-or-less random alloy, e.g. (Ga, Mn)N, in which Mn substitutes for one of the lattice constituents. The second class of approaches suggests that the magnetic atoms form small (a few atoms) clusters that produce the observed ferromagnetism. A difficulty in experimentally verifying the mechanism responsible for the observed magnetic properties is that, depending on the growth conditions employed for growing the DMS material, it is likely that one could readily produce samples that span the entire spectrum of possibilities from single-phase random alloys to nanoclusters of the magnetic atoms to precipitates and second-phase formation. Therefore, it is necessary to decide on a case-by-case basis which mechanism is applicable. This can only be achieved by a careful correlation of the measured magnetic properties with materials analysis methods that are capable of detecting other phases or precipitates. If, for example, the magnetic behaviour of the DMS is characteristic of that of a known ferromagnetic second phase (such as MnGa or Mn_4N in Ga, Mn)N [44]), then clearly the mean-field models are not applicable.

4. Role of second phases

There is clearly a need to examine the properties of (Ga, Mn)N with and without second phases, at least as detected by common analysis methods such as x-ray diffraction (XRD). The magnetic properties of (Ga, Mn)N grown by MBE in our group with a broad range of Mn concentrations (5 or 50 at.%) and which exhibited either one phase or multiple phases were examined. The first sample had a Mn concentration of ∼5 at.% as determined by both Auger electron spectroscopy and Rutherford backscattering. The growth conditions (temperature, rate and V/III ratio) were optimized to produce single-phase material. The second sample also had a Mn concentration of ∼5 at.%, but was grown under conditions where we observe second phases. The third sample had a Mn concentration of ∼50 at.% and was designed to contain large concentrations of second phases.

Figure 4 shows the resulting XRD powder scans from the three samples. Second-phase peaks are observed for the unoptimized 5 at.% Mn sample and the 50 at.% sample. In the optimized 5 at.% Mn material, only peaks due to hexagonal c-axis-aligned GaN and GaMn were observed. In separate experiments we have observed a linear variation in the (Ga, Mn)N lattice constant with Mn concentration, provided the material does not develop secondary phases. The only second phases observed in the unoptimized or high Mn concentration samples
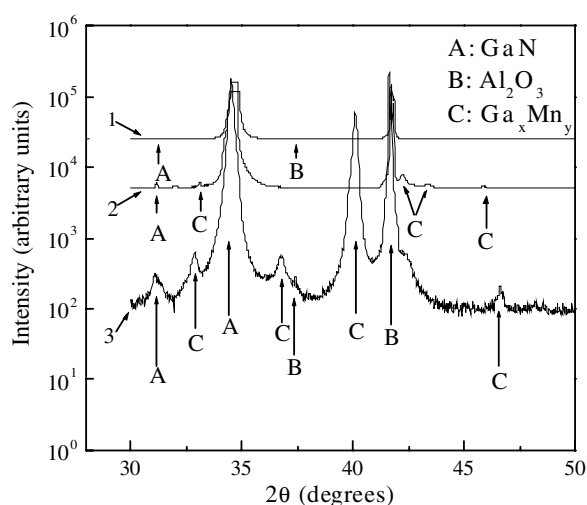
Figure 4. XRD scans from (Ga, Mn)N with either 5 at.% Mn (optimized growth, sample 1), 5 at.% Mn (unoptimized growth, sample 2) or 50 at.% Mn (sample 3).

are $Ga_x Mn_y$. Within this family of compounds, most are reported to be ferromagnetic in bulk form, namely Mn_2Ga ($T_C = 690$ K); Mn_3Ga ($T_C = 743$ K); Mn_5Ga_8 ($T_C \sim 210$ K) and MnGa ($T_C > 300$ K). We have not observed Mn_4N or other $Mn_x N_y$ phases under our growth conditions. In the growth of (Ga, Mn)N by MBE using a single precursor of ($Et_2Ga(N_3)NH_2CH_3$), the dominant second phase was Mn_3GaN ($T_C \sim 200$ K) [26].

All of the samples exhibited hysteresis in 300 K magnetization versus field loops (figure 5), with coercivities in the range of 100 G. A more instructive measurement is that of the temperature dependence of the field-cooled (FC) and zero-field-cooled (ZFC) magnetization, performed in a Quantum Design SQUID magnetometer. As shown in figure 6 (top), the single-phase (Ga, Mn)N is ferromagnetic to >300 K as shown by the separation in the FC and ZFC curves. In sharp contrast, the $x = 0.5$ sample shows behaviour typical of a spin glass at <100 K (figure 6 middle), while the multi-phase $x = 0.05$ material shows behaviour consistent with the presence of at least two ferromagnetic phases (figure 6 bottom). Note that the 50% sample still exhibits a loop at 300 K, indicating a small difference in FC and ZFC magnetization at this temperature. All of this behaviour is consistent with the XRD data.

What can be established from these experiments is that (Ga, Mn)N with 5 at.% Mn, grown by MBE under optimum conditions, shows no detectable second phases in x-ray diffraction spectra and exhibits ferromagnetism to >300 K. In material known to have second phases, the magnetization versus temperature behaviour shows either a spin-glass-type transition or cusps corresponding to the presence of multiple phases.

5. Electrical and optical properties

While a number of groups have reported room temperature ferromagnetism in GaN doped with Mn or Cr [31, 32, 34, 35], there has been little investigation of the electrical and optical properties of the material. The carrier-induced ferromagnetism model requires hole-induced interactions between the spins of the substitutional transition metal ions. However, the few reports of the position of Mn in the GaN bandgap find it to be very deep, $E_V + 1.4$ eV, where
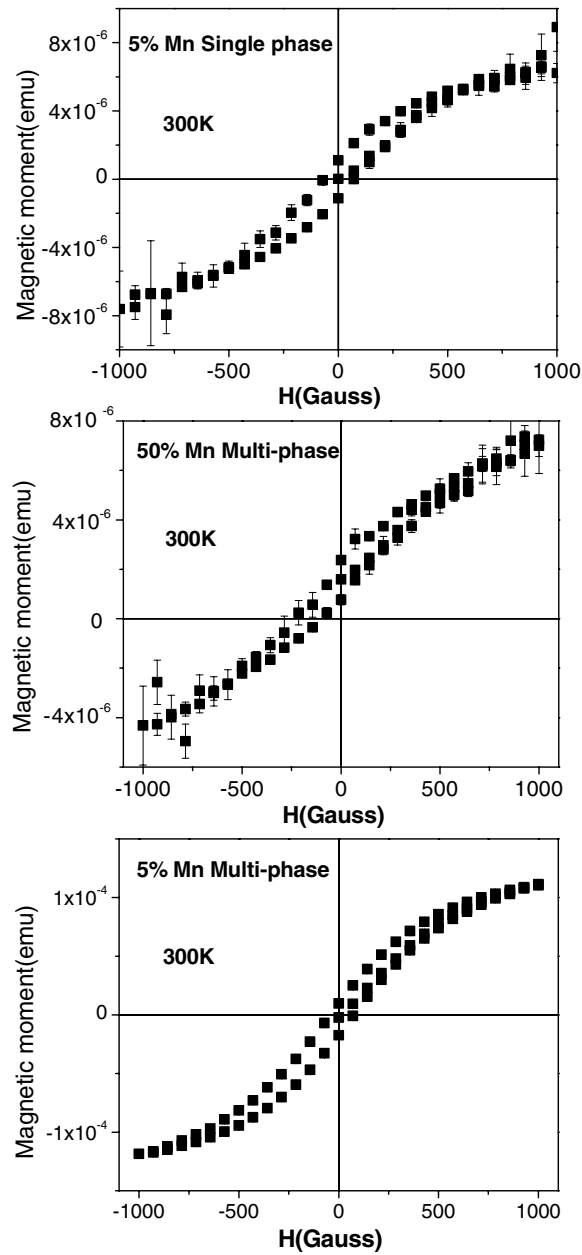
Figure 5. 300 K hysteresis loops for (Ga, Mn)N with 5 at.% Mn (optimized growth) at the top, 50 at.% Mn (in the middle) or 5 at.% Mn (unoptimized growth) at the bottom.

it would be an ineffective acceptor dopant [45–47]. In addition, most of the data reported for GaMnN indicate it is either insulating or n-type.

The resistivity of GaMnN grown by molecular beam epitaxy (MBE) in our group has been examined using both Schottky diode and transmission line method (TLM) measurements and optical absorption spectra from GaMnN films as a function of Mn concentration. Features at $E_C - 1.9$ eV are found in the absorption spectra, corresponding to transitions from Mn
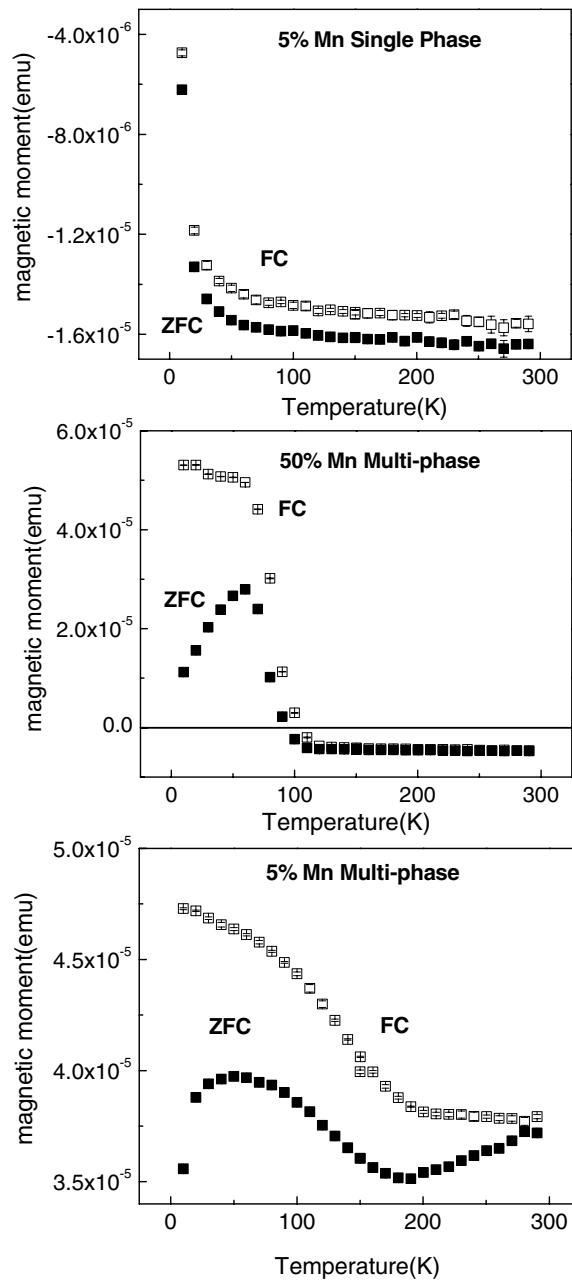
Figure 6. Temperature dependence of FC (top curve in each case) and ZFC (bottom curve in each case) magnetic moment for (Ga, Mn)N with 5 at.% Mn (optimized growth) at the top, 50 at.% Mn in the middle or 5 at.% Mn (unoptimized growth) at the bottom.

to the conduction band. However, this state does not control the Fermi level position in the GaMnN and the material remains high-resistivity n-type with a thermal activation energy of ~0.1 eV. The results have interesting indications for both the existing theoretical models for dilute magnetic semiconductors and for the potential technological uses of GaMnN.
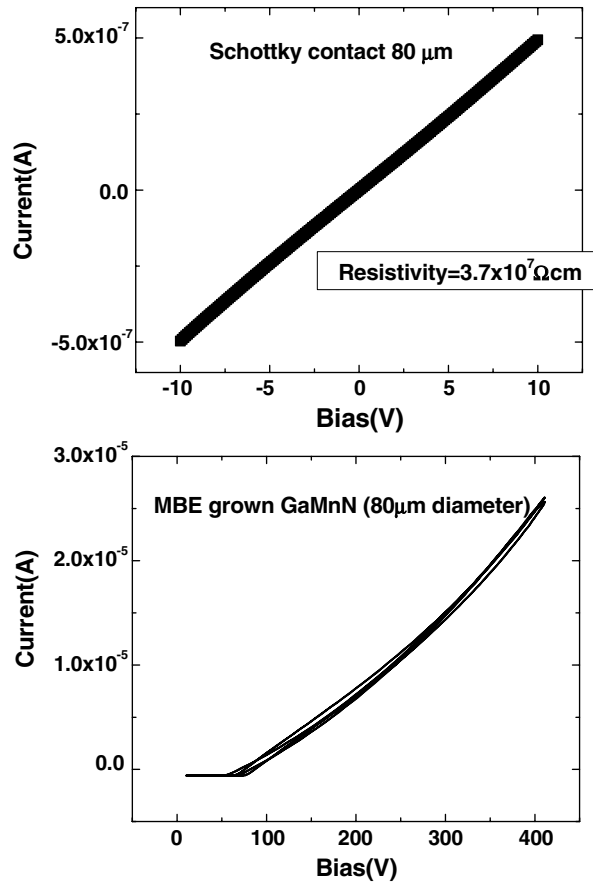
Figure 7. Low bias I–V characteristics at 25 °C from Schottky diode GaMnN/GaN structure (top) and forward I–V plots from several diodes at highest bias (bottom).

Figure 7 (top) shows the low bias I–V characteristics at 25 °C from the GaMnN/GaN device structure. The results are consistent with the GaMnN having a high resistance of $\rho = 3.7 \times 10^7\ \Omega$ cm. Even at higher biases, the I–V characteristic is dominated by the high resistance of the GaMnN (figure 7, bottom).

From TLM ohmic metal patterns placed directly on the GaMnN layer, we were able to measure the temperature dependence of the sheet resistivity. Figure 8 shows an Arrhenius plot of these data, corrected for the temperature dependence of the mobility contribution to the sheet resistivity. Over a broad range of temperature, the sheet resistivity varies as

$$\rho_S = \rho_{S0} \exp(-E_a/kT)$$

where $E_a = 0.11 \pm 0.02$ eV. This represents the activation energy of the defects or impurities controlling the n-type conductivity of the GaMnN.

These results are consistent with the absorption data. Figure 9 shows the spectral dependence of the absorption coefficient for GaMnN as a function of Mn concentration. The introduction of Mn produced an absorption band with a threshold near 1.9 eV which has been previously ascribed to transitions from Mn acceptors to the conduction band. We do not observe the band with a threshold near 1.4 eV corresponding to the transition from the valence band to the Mn acceptor, which is strong evidence for the sample being n-type with the Fermi
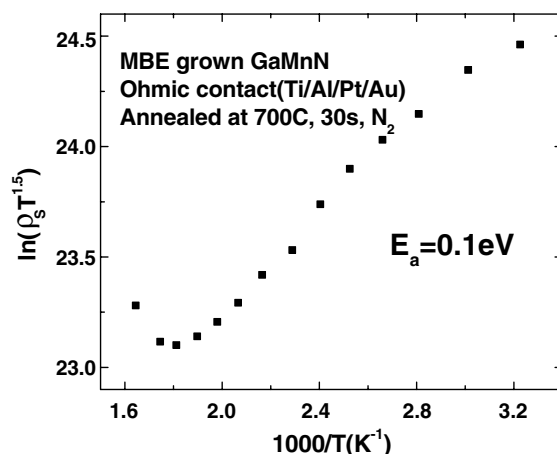
Figure 8. Arrhenius plot of sheet resistivity of the GaMnN layer, adjusted for the temperature dependence of mobility. The resulting activation energy is ~0.1 eV.
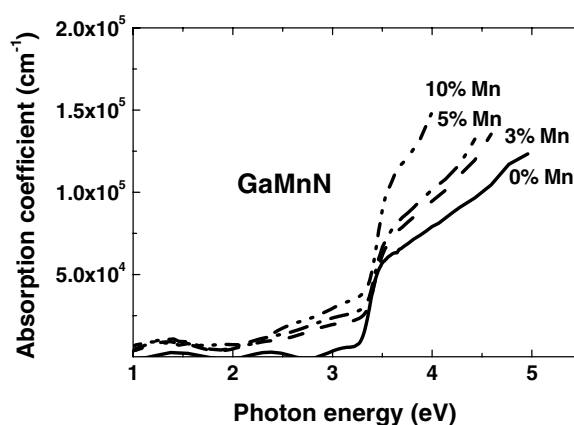

Figure 9. Optical absorption spectra from the GaMnN layer as a function of Mn concentration.

level in the upper level of the bandgap. Thus, even though there is a very high concentration of Mn acceptors in the GaMnN, these do not control the electrical properties of the materials. One possibility for the 0.1 eV donors are nitrogen vacancies.

Recent experiments on photoluminescence, optical absorption and photocapacitance spectra from Mn doped layers grown by metal–organic chemical vapour deposition (MOCVD) suggest that Mn forms a deep acceptor level in GaN near $E_V + 1.4$ eV [48–51]. However, Mn-implanted and annealed GaN films with Curie temperatures close to room temperature do not show the semi-insulating behaviour expected in such a case. Therefore some other defect centres must also be formed in high concentrations which contribute to conduction mechanisms in implanted films.

The optical transmission spectrum taken for the control sample (figure 10) showed a sharp edge near 3.4 eV and a dense pattern of interference fringes without any measurable absorption in the below-band-edge region. In contrast, the two Mn-implanted samples showed a strong absorption near 1.8 eV, i.e. close to the optical threshold for the transition from the $E_V + 1.4$ eV Mn acceptor level to the conduction band edge. For the Co-implanted sample the absorption
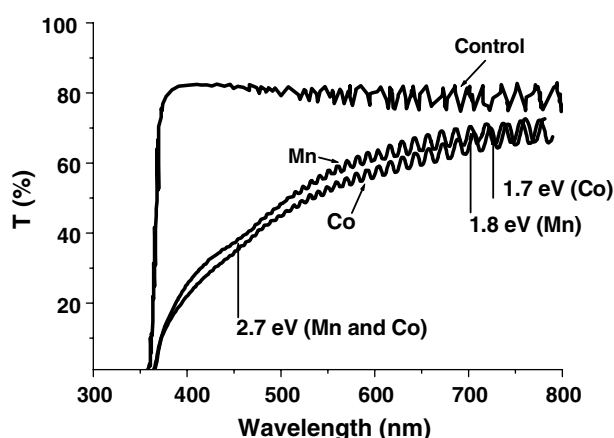
Figure 10. Optical transmission spectra at 300 K for the control sample, the 4×10^{16} cm^{-2} Mn-implanted sample and the 4×10^{16} cm^{-2} Co-implanted sample.

edge was slightly red-shifted to 1.7 eV, indicating the presence of a deep level about 0.1 eV deeper than the Mn acceptor.

Capacitance–voltage measurements on the unimplanted GaN gave an electron concentration of 2×10^{16} cm^{-3} and the intercept value in the $1/C^2(V)$ plot of 0.7 V, which is standard for Au Schottky diodes prepared on undoped n-GaN films grown by MOCVD. The frequency and temperature dependence of capacitance was very slight. The behaviour of the implanted samples was much more complicated. The capacitance at low frequencies was considerably higher than at high frequencies. At temperatures near 400 K the capacitance versus frequency curves showed well-defined low-frequency and high-frequency plateaux. At low frequencies the measured thickness of the space charge region was lower than 0.2 μm (i.e. the space charge region boundary was moving within the implanted region). The roll-off frequency in the low-frequency range decreased with decreased measurement temperature in a similar manner for all implanted samples and application of the standard admittance spectroscopy analysis to the shift in frequency with temperature yielded an activation energy of 0.45–0.5 eV. The $1/C^2(V)$ plots were linear for all three implanted samples, the apparent concentration deduced from the slope increasing from 6–8 $\times 10^{16}$ cm^{-3} for the Mn-implanted samples to 4.2×10^{17} cm^{-3} for the Co-implanted sample. Thus at these low frequencies the $C–V$ curves are determined by the uncompensated portion of the deep electron trap concentration with levels near $E_C - 0.5$ eV. These are most likely the traps responsible for the strong blue band in the MCL spectra and for the absorption band near 3 eV in figure 10 (the total concentration of these deep traps could be much higher than the value deduced from $C–V$ measurements since the latter relate to the uncompensated portion of the total density). No such centres were introduced in n-GaN upon implantation of protons and it seems reasonable to associate the observed centres with complexes of radiation defects with the transition metal acceptors.

Arrhenius plots of sheet resistance of the Mn-implanted (3×10^{16} cm^{-2}) GaN clearly showed more than one defect level present, producing a non-linear plot. The slopes at the two extremes of the plot corresponded to activation energies of 0.85 and 0.11 eV, respectively.

In figure 11 we compare the DLTS spectra for electron traps in the control sample and the 3×10^{16} cm^{-2} Mn-implanted sample. The Mn implantation greatly increases the density of the $E_C - 0.25$ eV electron traps and $E_C - 0.7$ eV electron traps known to be related to
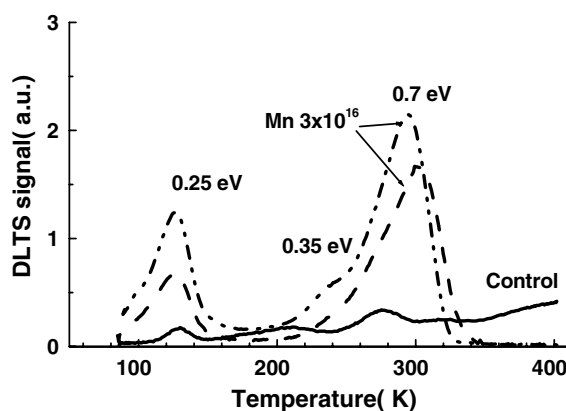
Figure 11. DLTS spectra of the control sample at -1 with $+1$ V forward pulse (full curve), of the 3×10^{16} cm^{-2} Mn-implanted sample taken with reverse bias of -1 V and forward bias of $+1$ V (short broken curve) and of the same sample measured with reverse bias of -3 V and forward bias of -1 V (broken curve).

point defects introduced, for example, during proton implantation into n-GaN. Moreover, the magnitude of the signal taken with a reverse bias of -1 V and forward bias of 1 V in the implanted sample was much higher than that taken with a reverse bias of -3 V and a forward bias pulse of -1 V. We attribute the difference to the fact that, in the former case, the space charge boundary during the injection pulse is pushed deeper into the damaged region where the density of deep radiation defects is higher. In figure 12 we compare the DLTS spectra of the Mn-implanted and Co-implanted samples taken under the same conditions. It can be seen that the concentration of radiation defects in the Co-implanted sample is considerably higher, most likely due to the higher initial density of the radiation defects in the region implanted with Co, Co being heavier than Mn. Our previous studies of the proton-implanted n-GaN samples have shown that the $E_C - 0.7$ eV radiation defects are very efficient lifetime killers which explains the extremely low photosensitivity of the Mn- and Co-implanted samples and the very low MCL intensity observed in these samples (the low photosignal and MCL signal was observed even with electron beam excitation with a beam energy of 25 kV when the excitation region penetrated much deeper than the projected Mn or Co ions' range of 0.2 μm, but not deeper than the thicker damaged region).

In figure 13 we show the optical DLTS spectra measured on the 3×10^{16} cm^{-2} Mn-implanted sample when the deuterium lamp UV source and the tungsten lamp visible light source were used. It can be seen that with the strongly absorbed UV light of the deuterium lamp the spectrum was dominated by electron traps with energies of 0.28 eV and an overlapping feature produced by the 0.35 and 0.5 eV electron traps. With the slightly absorbed visible light of the tungsten lamp the dominant features were the hole traps near $E_V + 0.2$, $E_V + 0.35$ and $E_V + 0.43$ eV. The results in the figure refer to the Mn-implanted sample but the only difference with the Co-implanted sample was the absence of the 0.35 eV electron trap peak in the D-lamp-excited spectrum. The difference might be due to the different penetration depth of the D lamp light compared to the W lamp light. In the first case electrons and holes are generated mainly in the near-surface-implanted region where a very high density of Mn or Co acceptors exist. The holes are effectively trapped by these acceptors and are disposed of by some very slightly activated process such as hopping via acceptor states with subsequent tunnelling at the Schottky diode. Thus only electron traps are left to be observed in the capacitance transients
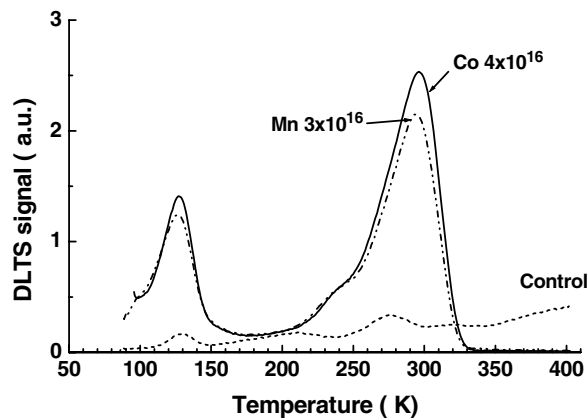
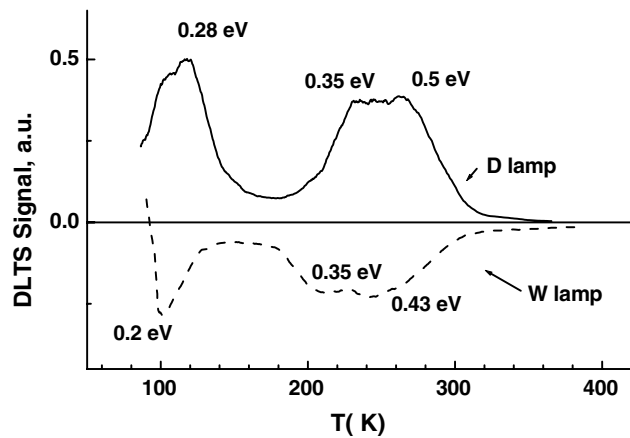**Figure 12.** DLTS spectra of the Mn-implanted (broken curve) and the Co-implanted (full curve) samples.

Figure 13. Optical DLTS spectra taken on the 3×10^{16} cm^{-2} Mn-implanted sample with D lamp and W lamp excitation.

and among them the 0.5 eV trap is the most likely one dominating the low frequency C–V characteristics and producing the blue MCL band.

We have shown that Mn implantation into GaN gives rise to a strong absorption with the threshold near 1.8 eV, which is close enough to the band observed in MOCVD-grown GaMnN samples in which Mn was shown to produce an acceptor level near $E_V + 1.4$ eV. The optical threshold for the Co-implanted sample was about 0.1 eV lower, implying that the Co acceptor level could be slightly deeper than the Mn level. This would be in line with general observations on the depth of the transition metals in III–V materials as a function of the d-shell filling: it has been noted that the higher the filling the deeper the level so that, in GaAs, the Mn acceptor is at $E_V + 0.1$ eV and the Co acceptor is at $E_V + 0.16$ eV, although for the wider bandgap GaP both dopants produce acceptor levels near $E_V + 0.4$ eV.

The fact that room temperature ferromagnetism can be achieved in n-type GaMnN is contrary to the main mean-field models, but is attractive from a technological viewpoint since most devices require either n-type material (i.e. field-effect transistors) or both n- and p-type

material (i.e. bipolar transistors and optical emitters). Further optimization of the growth conditions will be needed to reduce the unintentional donor concentration to the point where p-type GaMnN can be produced.

Other reports have also recently appeared on the magnetic properties of GaN doped with other transition metal impurities [31, 32, 34, 35, 48–51]. For initially p-type samples directly implanted with either Fe or Ni, ferromagnetism was observed at temperatures of $\sim$200 and 50 K, respectively. (Ga, Fe)N films grown by MBE showed Curie temperatures of $<$100 K, with EXAFS data showing that the majority of the Fe was substitutional on Ga sites [29]. (Ga, Cr)N layers grown in a similar fashion at 700 °C on sapphire substrates showed single-phase behaviour, clear hysteresis and saturation of magnetization at 300 K and a Curie temperature exceeding 400 K [51].

6. Transport properties

A key requirement for the successful realization of spin-based devices is an understanding of the transport properties within the dilute magnetic semiconductor, since carriers need to be injected from contacts and cross heterointerfaces in order to be collected. Some potential early demonstration devices include spin light-emitting diodes, in which injection and recombination of spin-polarized carriers could lead to polarized light emission, and spin transistors in which electron field gating can be used to control the carrier-induced ferromagnetism. Most GaN is still grown heteroepitaxially on lattice-mismatched substrates, such as sapphire, and therefore contains high concentrations (usually $\geqslant 5 \times 10^8$ cm^{-2} as measured by transmission electron microscopy, TEM) of threading dislocations and other extended defects. Numerous reports have demonstrated the deleterious effect of charged dislocations on the transverse carrier mobility in GaN. However, vertical devices are much less degraded by the repulsive band bending around dislocations and the directional dependence of the scattering due to these dislocations because of the greater average distance between defects in this geometry. This has been confirmed by an investigation of vertical and lateral transport in n-GaN films grown by our group, which showed vertical electron mobilities of $\sim$950 cm^2 V^{-1} s^{-1} compared to lateral mobilities of 150–200 cm^2 V^{-1} s^{-1}.

Hall measurements showed (Ga, Mn)N electron mobilities in the range of 102 cm^2 V^{-1} s^{-1} at 373 K to 116 cm^2 V^{-1} s^{-1} at 298 K. We believe these values are close to the true mobility in the (Ga, Mn)N, since measurements made on the GaN prior to Mn implantation showed much higher electron mobilities of $\sim$600 cm^2 V^{-1} s^{-1} at 298 K and thus, if most of the current was flowing in the buffer layer, we expect to measure an effective mobility closer to this value. This latter value of 600 cm^2 V^{-1} s^{-1} is similar to that reported for high quality n-type GaN.

To obtain the vertical mobilities, temperature-dependent I–V measurements were performed in the Schottky diode structures. The I–V characteristics on (Ga, Mn)N diodes measured from 298 to 373 K are shown in figure 14. The barrier heights (ϕ_B) extracted from the forward part of the I–V characteristics for both these and the diodes without Mn were obtained, with values ranging from 0.91 eV at 298 K to 0.88 eV at 373 K for the (Ga, Mn)N. By contrast, the measured barrier height on Pt/GaN diodes was 1.08 eV. The saturation current density, J_S, can be represented as

$$J_S = A^{**} T^2 \exp\left(-\frac{\phi_B}{kT}\right)$$

where A^{**} is the Richardson constant for (Ga, Mn)N, T is the absolute measurement
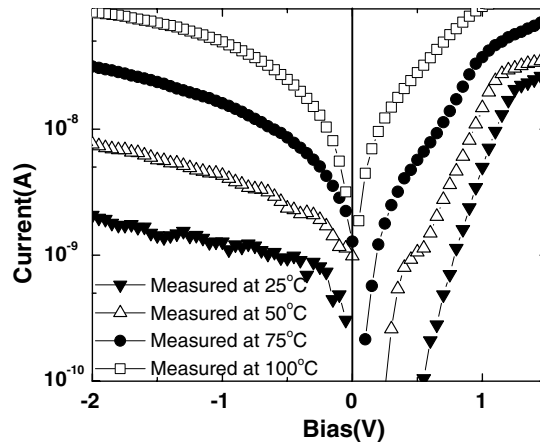
Figure 14. *I–V* characteristics as a function of temperature from n-(Ga, Mn)N Schottky diodes.
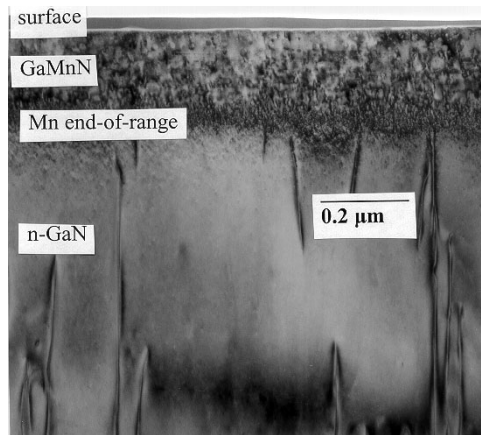

Figure 15. TEM cross section of (Ga, Mn)N layer formed in GaN by high dose Mn implantation.

temperature and k is Boltzmann's constant. This can also be written in the form

$$J_S = \left\{ e N_c \mu_{VERT} \left[\frac{2 e V_{bi} N_d}{\varepsilon} \right]^{1/2} \right\} \exp\left(\frac{-e\phi_B}{kT} \right)$$

where N_c is the effective density of states in the conduction band, μ_{VERT} is the electron mobility in the perpendicular direction, e is the electron charge, V_{bi} is the built-in voltage, ε is the dielectric constant and N_d is the doping density in the (Ga, Mn)N. The vertical values are factors of ∼3–8 higher at a given temperature than the lateral mobilities obtained from the Hall data. If the active area of the diodes is less than the geometric area then the effective vertical mobilities will be even higher than calculated here.

To give a visual representation of why the lateral mobility is more degraded by threading scattering than is the vertical mobility, figure 15 shows a cross-sectional TEM micrograph of the (Ga, Mn)N/GaN structure. Threading dislocations originating from the GaN/Al$_2$O$_3$ interface can reach the surface and therefore electrons travelling laterally through the structure encounter scattering from all of these defects. By contrast, for vertical transport, there is a relatively large fraction of nondefective material through which electrons can pass with undegraded mobility.
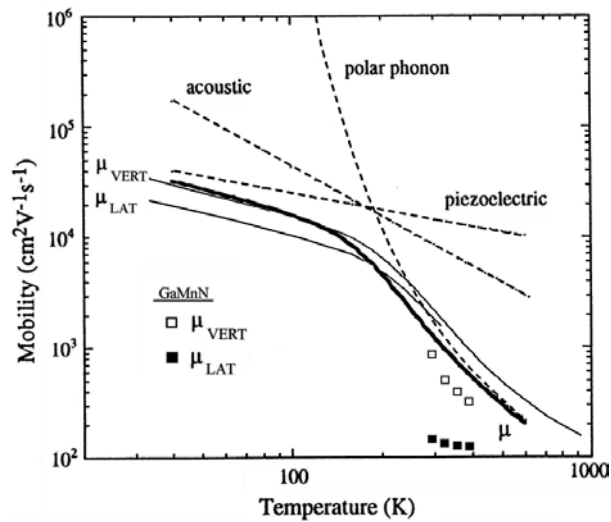
Figure 16. Theoretical drift mobilities in pure GaN, along with contributions from the various scattering processes present and the experimentally determined vertical and lateral mobilities for n-(Ga, Mn)N.

The defects remaining in the (Ga, Mn)N are mostly loops, which have only a second-order effect on the electrical properties, as reported previously for implanted GaAs.

To place the experimental data in context, figure 16 shows these results along with the calculated electron drift mobility of undoped GaN in both lateral and vertical directions and the individual components from the scattering processes (acoustic, polar phonon and piezoelectric) present. While no quantitative conclusions may be drawn, it is clear that the vertical and lateral mobilities are of comparable magnitude to those in material with minimal scattering. In the existing (Ga, Mn)N the vertical electron mobility is relatively unaffected by charge dislocation scattering and gives an indication of the values that it will be possible to achieve for lateral electron mobilities in material synthesized on low defect GaN such as free-standing quasi-substrates.

In summary, the effect of dislocation scattering on electron mobility in (Ga, Mn)N has been examined through a comparison of vertical and lateral transport properties. The vertical electron mobilities are found to be a factor of 3–8 higher than the corresponding lateral mobilities at the same temperature. (Ga, Mn)N-based spintronics devices with vertical geometries will be at an advantage relative to lateral devices.

7. Contacts to (Ga, Mn)N

One of the possible applications of dilute magnetic semiconductors is in so-called spin field effect transistors (spin FET) in which electric field gating is used to control the carrier-induced ferromagnetism. This has already been demonstrated in metal–insulator–semiconductor (MIS) structures based on (In, Mn)As at 10 K. Therefore it is necessary to understand the properties of rectifying contacts on (Ga, Mn)N as a first step towards realizing practical spintronics switches.

From the I–V–T characteristics of Pt Schottky diodes on n-type (Ga, Mn)N synthesized by our group, we extracted a value for the Richardson constant for this material of A^{**} of 91.2 A cm^{-2} K^{-2}, but there is a large uncertainty ($\sim\pm60\%$) in this due to the narrow

range of measurement temperatures from which we had to extrapolate to obtain the estimated Richardson constant. For comparison, a similar analysis for Pt/n-GaN Schottky diodes reported values of 64.7–73.2 for A^{**}.

From the measured $I–V$ characteristics at each temperature we were able to extract the ϕ_B values for Pt on (Ga, Mn)N. The barrier height at 25 °C was 0.82 ± 0.04 eV, which compares to a value of 1.08 eV for Pt on n-GaN determined from $I–V$ characteristics. It should also be noted that, in the early stage of developing a new materials system, it is common to have a wide range of values reported for barrier heights due to the presence of surface defects, interfacial layers and material inhomogeneities. The barrier height was also extracted from the activation energy plots in the measured $I–V–T$ data and the saturation current at each temperature. The plot of $\ln(I_S/AT^2)$ versus inverse temperature yielded a barrier height of 0.91 ± 0.06 eV, which is consistent with the value at 25 °C derived from the forward $I–V$ characteristics.

The reverse leakage of the diodes was found to depend on both bias and temperature. From a moderately doped sample of the type studied here, we would expect thermionic emission to be the dominant leakage current mechanism. According to image–force barrier height lowering, this leakage current density, J_L can be written as

$$J_L = -J_S \exp\left(\frac{\Delta\phi_B}{kT}\right)$$

where $\Delta\phi_B$ is the image–force barrier height lowering, given by $(\frac{eE_M}{4\pi\varepsilon_S})^{1/2}$, where E_M is the electric field strength at the metal/semiconductor interface and ε_S is the permittivity. The experimental dependence of J_L on bias and temperature is stronger than predicted from this equation. The large bandgap of (Ga, Mn)N makes the intrinsic carrier concentration in a depletion region very small, suggesting that contributions to the reverse leakage from generation in the depletion region are small. Therefore, the additional leakage must originate in contributions from other mechanisms such as thermionic field emission or surface leakage.

8. AlN-based ferromagnetic semiconductors

AlN plays an important role in many areas of solid-state devices [52–67], including thin film phosphors, nitride-based metal–insulator–semiconductor heterostructure transistors, thin-film gas sensors, acoustic wave resonators, UV light-emitting diodes, distributed Bragg reflectors, heat spreaders and heterojunction diodes. AlN may also be promising in the emerging field of spintronics, due to its predicted high Curie temperature (T_C) when doped with particular transition metals. Room temperature ferromagnetism has been reported for Cr-doped AlN thin films deposited by reactive sputtering [52] or molecular beam epitaxy [53]. Ion implantation provides a versatile and convenient method for introducing transition metals into semiconductors for examination of their effects on the structural and magnetic properties of the resulting material [68]. AlN is an ideal host in this regard, since Kucheyev *et al* [69] reported that single-crystal epilayers of AlN grown on sapphire substrates did not become amorphous even at LN_2 temperatures for high doses of kiloelectronvolt heavy ions such as Au. In addition, very high quality AlN on sapphire has recently been reported by several groups [70, 71], providing well-characterized material in which to examine the properties of transition metals. The fabrication of ferromagnetic AlN would create a wider range of possible all-semiconductor spin-dependent devices. For example, ferromagnetic AlMnN could be used as a magnetic barrier in a tunnel junction where it would serve as a spin filter. The predicted Curie temperature of AlMnN is greater than 300 K and recently a Curie temperature of more than 340 K has been observed for AlN:Cr [52, 53].
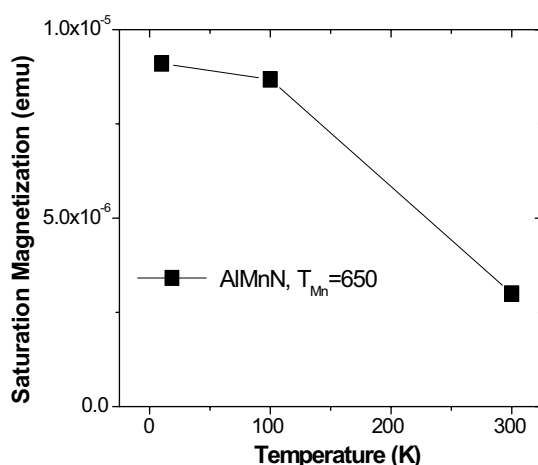
Figure 17. Saturation magnetization versus temperature for single-phase AlMnN grown at 650 °C. Saturation magnetization was extracted from SQUID hysteresis loops.

Growth of the films was carried out in our group by gas-source molecular beam epitaxy. Solid Al(7N) and Mn(7N) sources were heated in standard effusion cells. Gaseous nitrogen was supplied by an Oxford rf plasma head. All films were grown on (0001) oriented sapphire substrates, indium-mounted to Mo blocks. AlMnN and AlN films were grown at a temperature of 780 °C, as indicated by the substrate heater thermocouple. Sapphire substrates were first nitridated for 30 min at a substrate temperature of 1000 °C under 1.1 sccm nitrogen (chamber pressure = 1.9×10^{-5} Torr). Nucleation at 575 °C for 10 min and a 30 min buffer layer at 950 °C followed nitridation, both under 1.1 sccm nitrogen. Both AlN and AlMnN films were grown with a substrate temperature of 780 °C and an Al effusion cell temperature of 1150 °C. The Mn cell temperature was varied from 635 to 658 °C. The growth rate of the AlN was 0.2 μm h^{-1} and the growth rate of the AlMnN films was 0.16 μm h^{-1}.

In situ reflection high energy electron diffraction (RHEED) was used to monitor films during growth. AlN demonstrated 2D growth and AlMnN films demonstrated 2D/3D growth. AlMnN grown with a Mn cell temperature of 635 °C was found to be single phase. The AlMnN with $T_{Mn} = 658$ °C formed AlMn as detected by powder XRD. A Mn cell temperature of 650 °C was found to be the upper limit of single-phase AlMnN under previously mentioned growth conditions. For comparison, a layer of Mn$_4$N was also grown on sapphire.

The lattice constant was found to decrease as the Mn cell temperature increased for single-phase material. A similar pattern was observed for single-phase GaMnN films grown in the same system under different conditions. GaN implanted with Mn has been reported to exhibit substitutional or near-substitutional incorporation. It is expected that the incorporation of interstitial Mn should either increase or have no effect on the lattice constant. The observation of a decrease in the lattice constant of the AlMnN films suggests that the Mn occupies a substitutional site. This is further confirmed by Hall analysis, which showed pure AlN to be highly resistive as expected and material containing an AlMn second phase to be highly conductive n-type. In contrast, single-phase AlMnN was found to be p-type. If Mn incorporates substitutionally, one would expect by analogy with its behaviour in other III–V materials that it would behave as a deep acceptor. The observation of p-type behaviour fits this explanation.

Magnetic remanence and coercivity indicating hysteresis was observed in ternary AlMnN films at 10, 100 and 300 K (figure 17). Measurements over 300 K were not possible due to
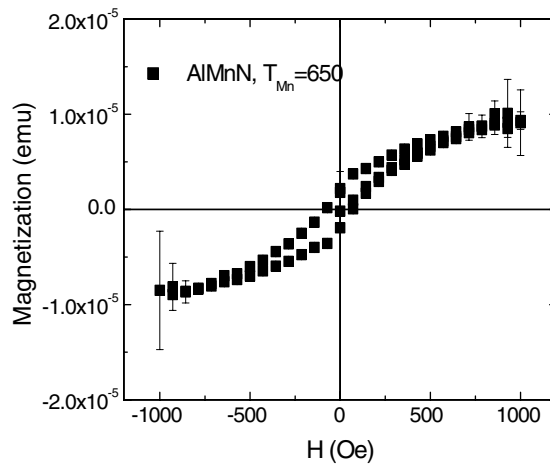
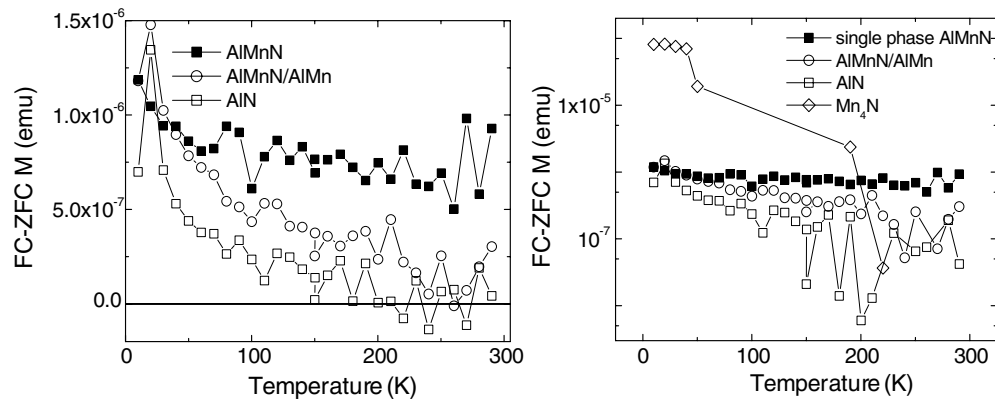**Figure 18.** Magnetization versus applied field for single-phase AlMnN.

Figure 19. Magnetization versus temperature for AlN, AlMnN, Mn_4N and AlMnN/AlMn. The magnetic signal is determined by subtracting the zero-field-cooled trace from the field-cooled curve.

limitations in the magnetometer. Saturation magnetization was found to decrease at 300 K compared to 100 K for AlMnN grown at $T_{Mn} = 650\,°C$. The values of temperature-dependent saturation magnetization of AlMnN are shown in figure 18. These data indicate an approaching T_C for this material. However, hysteresis persisted to 300 K, demonstrating soft ferromagnetism at room temperature. Figure 19 depicts the field dependence of magnetization for AlMnN and AlN films. Pure AlN grown under the same conditions as AlMnN demonstrated paramagnetic behaviour. This indicates that ferromagnetism arises with the addition of Mn. The diamagnetic background due to the sapphire substrate was subtracted from the raw data and the subsequent corrected data was used for analysis. The magnetization was not normalized to the Mn concentration due to the difficulty in calculation of the precise amount of Mn in the films. Perpendicular measurements were found to have lower values for saturation magnetization in AlMnN films.

The hysteresis observed in the AlMnN is believed to arise from the inclusion of Mn into the AlN lattice. Clusters of second phases, undetectable by the methods mentioned above, are not thought to be the cause of ferromagnetism observed at 300 K. This is supported by magnetic
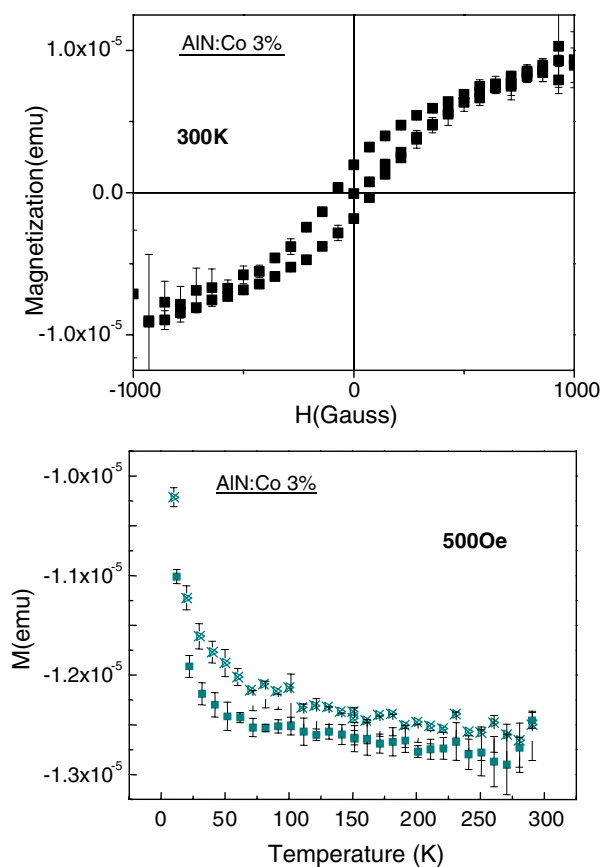
Figure 20. 300 K magnetization as a function of field (top) and FC and ZFC magnetization as a function of temperature (bottom) for AlN implanted with 3×10^{16} cm^{-2} Co^{+} and annealed at 950 °C, 2 min.

analysis of material containing the most likely cluster phases, AlMn and Mn$_4$N. Magnetization as a function of temperature for AlN, single-phase AlMnN, AlMnN with an AlMn phase present and Mn$_4$N show substantially different behaviour, as shown in figure 20. The reason for the low T paramagnetic behaviour seen in AlN and AlMnN films is still unknown. The M versus T of Mn$_4$N clearly indicates ferromagnetic behaviour and the formation of clusters has been proposed as the cause of hysteresis in some ferromagnetic III–V materials. However, the formation of Mn$_4$N clusters does not influence the magnetization above 250 K, since clearly the magnetization drops to zero at that temperature. Also, the magnetization versus temperature indicates that the formation of AlMn clusters is not the cause of the ferromagnetism observed, shown by the order-of-magnitude difference between the values of magnetization over 150 K. Hence, the incorporation of Mn into the AlN lattice forming the ferromagnetic ternary AlMnN is most likely the reason for the observed hysteresis.

9. Implanted AlN films

Ferromagnetism has also been observed in transition-metal-implanted films. Implantation of Cr^{+}, Co^{+} or Mn^{+} ions was carried out at an energy of 250 keV (corresponding to a projected range of ∼1500 Å in each case) and a fixed dose of 3×10^{16} cm^{-2}. As a rough

guide, the peak transition metal concentrations, located at the projected range, are ∼3 at.% in the AlN. After implantation, the samples were annealed at 950 °C, 2 min under flowing N_2. Photoluminescence (PL) measurements were carried out with a quadrupled Ti:sapphire laser as an excitation source together with a streak camera, providing an excitation power of ∼3 mW at 196 nm [72].

PL spectra taken at 10 K of the AlN implanted with Cr, Mn or Co after annealing at 950 °C for 2 min looked basically identical in each case, even without annealing. The unimplanted AlN showed strong band-edge emission at ∼6.05 eV and two broad emission bands related to deep level impurities at ∼3.0 and 4.40 eV, each of which had a peak intensity of ∼1% of the band-edge emission intensity. The Cr-, Mn- and Co-implanted AlN showed an absence of band-edge emission, which suggests that the point defect recombination centres created during implantation are stable against annealing at 950 °C.

Well-defined hysteresis was present in the Co-implanted AlN, with a coercive field of ∼160 Oe at 300 K and 230 Oe at 10 K. The diamagnetic contributions from the substrate have been subtracted out of the data. At 300 K, the saturation moment, $M_O = g\mu_B S$, where g is the degeneracy factor, μ_B is the Bohr magneton and S is the total number of spins, was calculated to be ∼0.65 μ_B for Cr. This value is lower than the theoretical value of 3 μ_B expected for a half-filled d band of Cr, if all of the Cr ions were participating in the ferromagnetic signal. Disorder effects due to implantation-induced change, may contribute to creating a distribution of exchange couplings that favour antiferromagnetism and reduce the effective magnetism.

Similar data are shown in figure 21 for the Co-implanted AlN. Once again there is hysteresis present at 300 K, with a coercive field of ∼1750 Oe at 300 K and 240 Oe at 100 K and a calculated saturation moment of 0.52 μ_B for Co. The FC and ZFC magnetization versus temperature values are shown at the bottom of the figure. In this case the differences extend to ∼100 K.

Figure 22 (top) shows magnetization versus field at 100 K for Mn-implanted AlN. This was the highest temperature for which clear hysteresis could be obtained. The coercive field was ∼220 Oe at both 100 and 10 K. The FC and ZFC phases are almost coincident at an applied field of 500 Oe, as shown at the bottom of the figure and consistent with lower overall magnitude of the magnetization. The calculated saturation moment was 0.17 μ_B for Mn at 100 K, compared to the theoretical value of 4.

The main θ–2θ XRD peaks of the Cr- or Mn-implanted samples after 950 °C annealing correspond to the expected AlN(0002) and (0004) lines and Al_2O_3(0002), (0006) and (0012) substrate peaks and the broad peak at $2\theta = 20°$ is due to short-range disorder from the implantation process and was not observed on the as-grown films. No peaks due to the half-metallic ferromagnetic CrO_2 phase were detected in the Cr-implanted sample and other potential second phases which could form, such as Cr, CrN [73–75], Cr_2N and Al_xCr_y, were not detected and in any case are not ferromagnetic at the temperatures used in these experiments. Similarly, in the case of Co implantation, metallic Co has a Curie temperature of 1382 K and Co_xN phases are all Pauli ferromagnetic. Finally, for Mn implantation, metallic Mn is antiferromagnetic while Mn_xN is ferromagnetic with a Curie temperature of 745 K. Thus, secondary ferromagnetic phases are not responsible for the observed magnetic properties.

The origin of the observed ferromagnetism is not likely to be carrier-mediated due to the insulating nature of the AlN. Wu *et al* [53] suggested that substitutional $Al_xCr_{1-x}N$ random alloys would have Curie temperatures over 600 K, as estimated from a multi-component mean-field theory in which the ferromagnetism occurs in a midgap defect band. Another possible mechanism for the observed magnetic properties is that the Mn is not randomly distributed on Al sites but is present as atomic scale clusters. Some mean-field theories suggest that Mn clustering can significantly influence T_C as a result of the localization of spin polarized holes
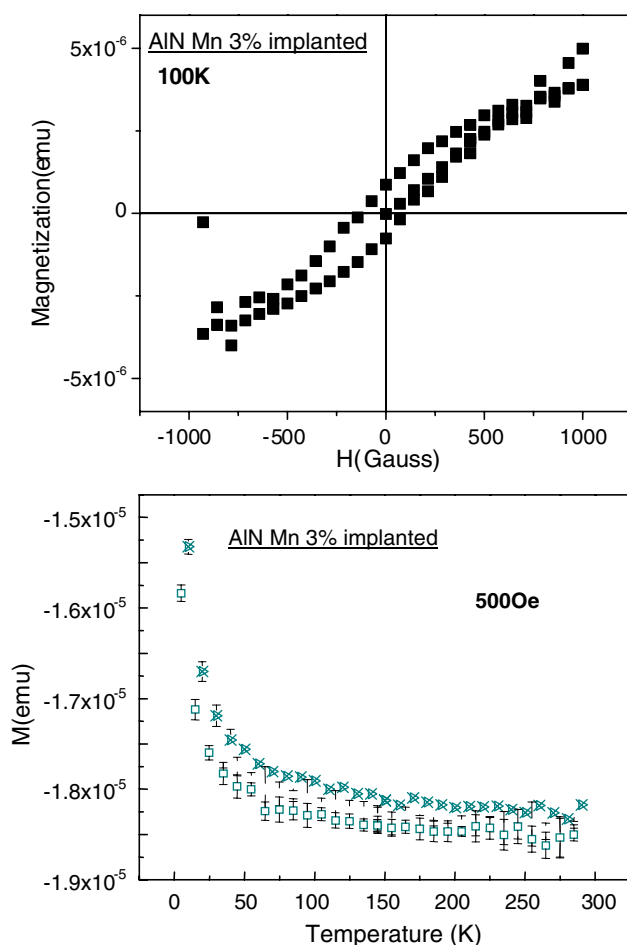
Figure 21. 100 K magnetization as a function of field (top) and FC and ZFC magnetization as a function of temperature (bottom) for AlN implanted with 3×10^{16} cm^{-2} Mn$^+$ and annealed at 950 °C, 2 min.

near regions of higher Mn concentration. There is also some support for this assertion from local spin density approximation calculations which predict it is energetically favourable for the formation of magnetic ion dimers and trimers at second-nearest-neighbour sites which are ferromagnetic. The percolation-network-like model for ferromagnetism in low carrier concentration systems suggested by several groups is another potential mechanism.

High doses (3×10^{16} cm^{-2}) of ion-implanted Co$^+$, Cr$^+$ or Mn$^+$ ions into AlN epi layers on Al$_2$O$_3$ substrates severely degrades the band-edge luminescence, which is not recovered by annealing up to 950 °C. In each case the implanted AlN shows ferromagnetic ordering, as evidenced by the presence of hysteresis in the M versus H loops. The hysteresis persists up to $\geqslant$300 K in the case of Cr$^+$ or Co$^+$ implantation and 100 K for Mn$^+$ implantation. Less than $\sim$20% of the implanted ions contribute to the magnetization, but this might be increased by the use of much higher annealing temperatures. Simple two-terminal resistivity measurements show that the implanted AlN remains insulating ($>$10^8 Ω cm) and thus conventional carrier-mediated ferromagnetism is not a likely mechanism for the observed magnetic properties.
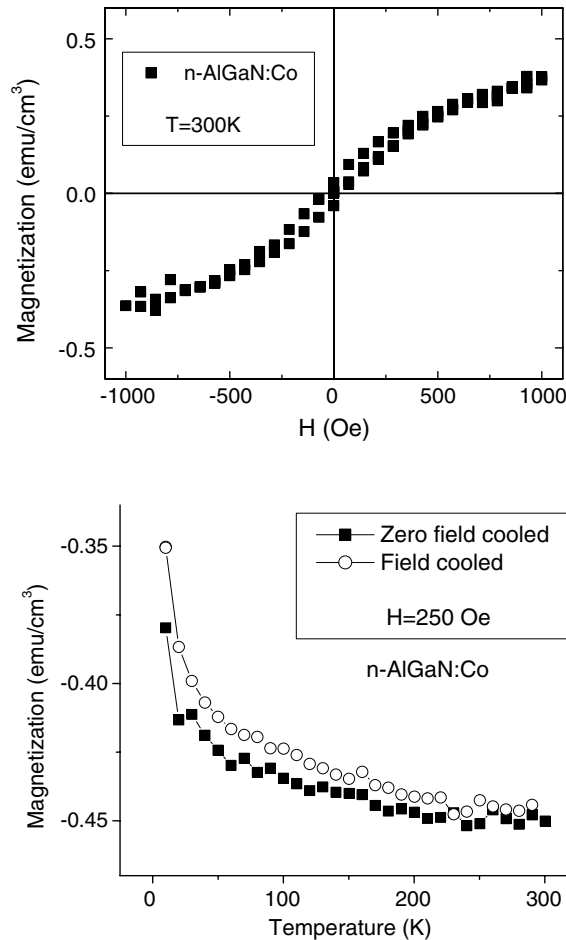
Figure 22. 300 K magnetization as a function of field (top) and field-cooled (FC) and zero-field-cooled (ZFC) magnetization (bottom) versus temperature for AlGaN implanted with 3×10^{16} Co$^+$ annealed at 1000 °C for 2 min.

Implantation provides a versatile method of introducing different transition metal dopants into AlN for examination of their effect on the structural and magnetic properties.

10. Implanted AlGaN films

There is also interest in the use of transition-metal-doped AlGaN for possible applications in spintronic devices such as polarized light emitters or spin transistors. The latter exploits quantum interference effects provided electrons with a particular spin can be injected into the channel of the device and a gate bias can be applied to cause splitting of spin-up and spin-down states. A key requirement for spin-based semiconductor devices is the achievement of ferromagnetism, preferably above room temperature. The properties of implanted transition metals in AlGaN is of particular relevance for the realization of polarized light emitters or spin transistors since it could serve as the cladding layer in the former and the wide bandgap part of the heterostructure in the latter.
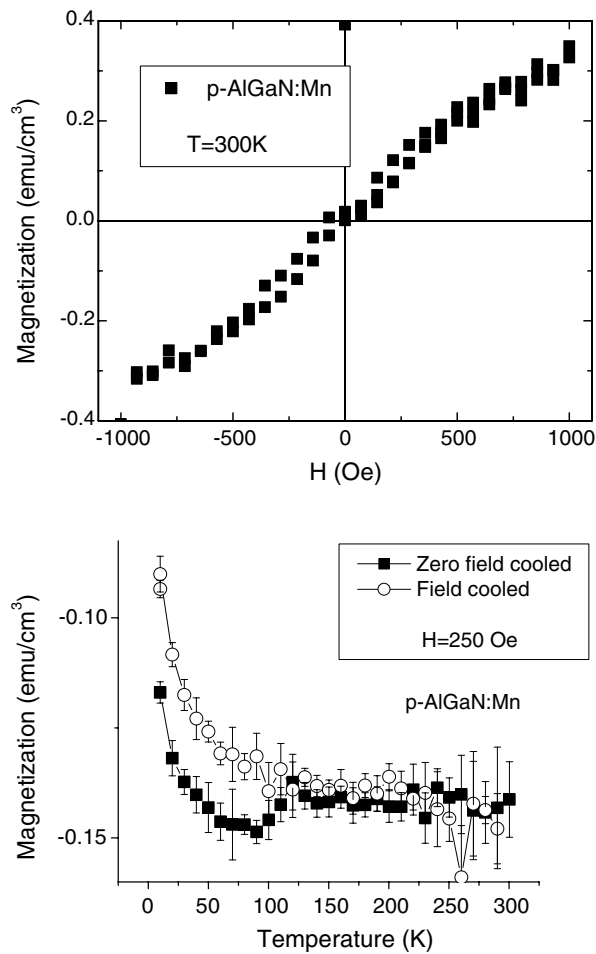
Figure 23. 300 K magnetization as a function of field (top) and field-cooled (FC) and zero field-cooled (ZFC) magnetization (bottom) versus temperature for AlGaN implanted with 3×10^{16} Mn$^+$ annealed at 1000 °C for 2 min.

θ–2θ XRD scans from the n-AlGaN grown by our group before and after Mn$^+$, Co$^+$ or Cr$^+$ implantation and annealing at 1000 °C did not show any observable differences. The highest intensity peaks in all spectra correspond to the expected AlGaN(0002) and (0004) lines and Al$_2$O$_3$(0002), (0006) and (0 0 0 12) substrate peaks. We did not observe any peaks due to second phases that could exhibit ferromagnetism. For example, in the Mn-implanted material, Mn$_x$N is ferromagnetic with a Curie temperature of 745 K and GaMn is also ferromagnetic with a Curie temperature near 300 K (metallic Mn is antiferromagnetic). In the Co$^+$-implanted AlGaN, metallic Co has a Curie temperature of 1382 K and Co$_x$N phases are all Pauli ferromagnetic. Finally, in the Cr$^+$-implanted AlGaN, CrO is half-metallic, while Cr, CrN, Cr$_2$N, Al$_x$Cr$_y$ and Ga$_x$Cr$_y$ are not ferromagnetic [36]. However, in such thin layers, it could be possible for small quantities of second phases to be present and remain undetectable by XRD.

Well-defined hysteresis at 300 K was observed for the Co-implanted Al$_{0.38}$Ga$_{0.62}$N, as shown at the top of figure 23. The coercive field was ~85 Oe at 300 K and ~75 Oe at 10 K. The saturation magnetization was ~0.4 emu cm^{-3} or ~0.76 μ_B calculated saturation
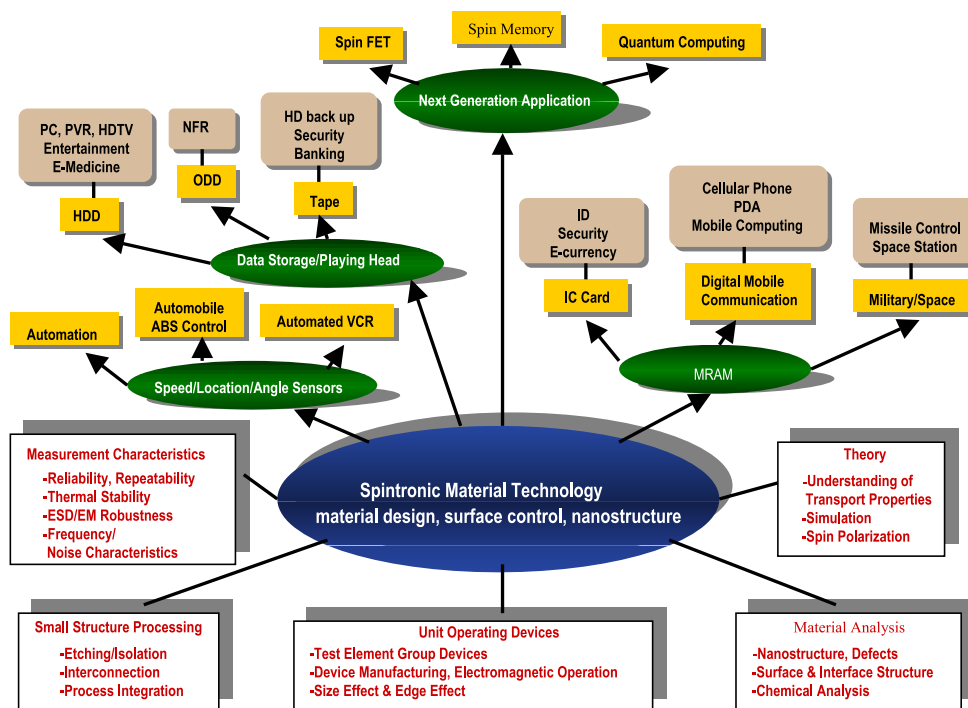
Figure 24. Projected technology tree for semiconductor spintronics (after
http://spintronics.korea.ac.kr/research_map1.htm).

moment. This is slightly higher than the value reported for Co^+ implantation into pure AlN under similar conditions ($0.52\,\mu_B$), which is consistent with the higher vacancy concentrations expected to be created in AlGaN due to its lower bond strength. The bottom part of figure 23 shows the temperature dependence of field-cooled (FC) and zero field-cooled (ZFC) magnetization for the Co^+-implanted AlGaN. The fact that these have different values out to ~230 K is a further indication of the presence of ferromagnetism in the material. In both epitaxial and ion-implanted transition-metal-doped semiconductors, we have found the general result that the hysteresis can be detected to higher temperatures than the difference in FC and ZFC magnetization. As mentioned earlier, the samples exhibited low carrier densities ($< 3 \times 10^{16}$ cm^{-3} from Hall measurements) after implantation and annealing and therefore carrier-mediated ferromagnetism by free electrons is not expected to be operative. In addition, the Co ionization level is expected to be deep in the AlGaN bandgap, so that there will be no significant contribution to the carrier density from the substitutional fraction of these atoms. More recent percolation network models for ferromagnetism in dilute magnetic semiconductors suggest that localized carriers may mediate the interaction between magnetic ions in low carrier density systems.

The Mn-implanted p-type AlGaN also showed a well-defined hysteresis loop at 300 K, with a coercivity of ~60 Oe (figure 24, top). The saturation moment, $M_0 = g\mu_B S$, where g is the degeneracy factor, μ_B is the Bohr magneton and S is the total number of spins, was calculated to be ~$0.57\,\mu_B$. The theoretical value would be 4 if all of the implanted Mn was participating towards the ferromagnetism, so the lower experimental value indicates that only a fraction of the Mn is substitutional and magnetically active. The saturation moment for AlGaN is significantly larger than the value of $0.17\,\mu_B$ reported for Mn implantation into pure AlN.

The temperature dependence of FC and ZFC magnetization is shown at the bottom of figure 24. The ferromagnetism is very weak above ~125 K but is detectable through the hysteresis.

In sharp contrast to the case of Mn implanted into p-AlGaN, when we performed the same implants into n-AlGaN the resulting differences in FC and ZFC magnetization were very weak and hysteresis loops, even at 10 K, did not show clear evidence of ferromagnetism. The differences from the p-type material may result from the higher AlN mole fraction in the n-type AlGaN, which makes it harder for the implanted ions to become substitutional upon annealing. An alternative explanation is that holes are more efficient at ferromagnetic coupling between the Mn spins than are electrons. This has been reported previously for both n- and p-type GaAs and GaP doped with Mn. We also did not observe any clear evidence for ferromagnetism in the Cr-implanted n-AlGaN. This is a clear difference from the case of Cr-implanted AlN, where hysteresis was reported at 300 K.

In conventional dilute magnetic semiconductors such as (Ga, Mn)As, the magnetization is given by [11]

$$M = \mu_g \mu_B S N_0 x_{\text{eff}} B_S \left[\frac{g\mu_B(-\partial F_C[M]/\partial M + H)}{k_B(T + T_{\text{AF}})} \right]$$

in the mean-field approach, where S is the localized spin, N_0 is the concentration of cation sites, X_{eff} is the effective spin concentration, B_S is the Brillouin function and $F_C(M)$ is the hole contribution to the free-energy functional F (which depends on the magnetization of the localized spin). The validity of this model depends on having a high carrier concentration in the magnetic semiconductor and experimentally we do not observe this in the AlGaN and correspondingly we do not observe a Brillouin-like dependence of magnetization on temperature. In pure AlN, Mn produces an absorption line at ~1.5 eV from the valence band, suggesting the $Mn^{3+/2+}$ acceptor level is deep in the gap and makes the realization of carrier-mediated ferromagnetism unlikely. The mean-field models have also shown that Mn clustering can enhance the Curie temperature through localization of localized carriers at these clustered regions. Some calculations suggest it is energetically favourable to form ferromagnetic transition metal ion dimers and trimers at second-nearest-neighbour sites. Distant pairs would be weakly ferromagnetic or antiferromagnetic. These predictions suggest that the ferromagnetism will be a very strong function of the synthesis conditions used for the magnetic semiconductor. They also suggest that non-equilibrium methods such as ion implantation possess inherent advantages in trying to maximize the Curie temperature because of their ability to achieve solid solubilities for dopants well above those possible with equilibrium synthesis methods.

11. Potential device applications

Previous articles have discussed some spintronic device concepts such as spin junction diodes and solar cells, optical isolators and electrically controlled ferromagnets [76–80]. The realization of light-emitting diodes with a degree of polarized output has been used to measure spin injection efficiency in heterostructures. While the expected advantages of spin-based devices include non-volatility, higher integration densities, lower power operation and higher switching speeds, there are many factors still to consider in whether any of these can be realized. These factors include whether the signal sizes due to spin effects are large enough at room temperature to justify the extra development work needed to make spintronic devices and whether the expected added functionality possible will materialize.

There are already many different uses for spintronics based on magnetic multi-layers, including hard drives for personal computers, non-volatile magnetic random access memories

**Spin FET on silicon
(Datta-Das Configuration)**
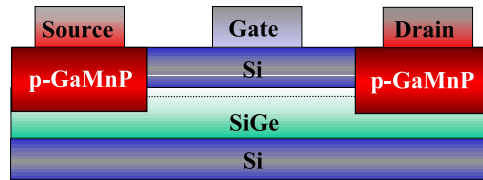
N-type version possible using strained Si
on SiGe strain relief buffer

Figure 25. Schematic of Si-based spin FET.

(MRAM) and magnetic sensors, as shown in figure 24. The basic idea behind semiconductor-based spintronics is to add the characteristics of magnetic devices to existing devices such as light-emitting diodes and field effect transistors. This would lead to technologies such as memory and microprocessor functions integrated on the same chip, magnetic devices with gain and integrated sensors with on-chip signal processing and off-chip optical communications. There may also be a use for spins in semiconductor quantum dots or wells in realizing a practical quantum computer. In a so-called spin qubit, the electron spin is used as a quantum bit, i.e. a bit that can exist as a superposition of a pure '0' state and a pure '1' state. Electron spins are natural qubits because any electron spin state is always a superposition of a spin up ('1') and a spin down ('0') state.

One of the suggested prototype spin devices is the so-called spin FET. A possible embodiment is illustrated in figure 25. In this device, carriers are injected from a magnetized source contact (which can be either a ferromagnetic metal or a dilute magnetic semiconductor) through a channel to be collected at a drain contact that is magnetically aligned with the source contact. Without any bias voltage applied to the gate, the polarized carriers are collected at the drain contact. This is the same mechanism of operation as in a conventional charge-controlled FET. In a spin FET, application of a relatively low gate voltage causes an interaction between the electric field and the spin precession of the carriers. If this is sufficient to put the spin orientation of the carriers out of alignment with the drain contact, then the current is effectively shut off and this can occur at much lower biases than is needed to shut off the current in a charge-controlled FET. In figure 25, we show a schematic of a Si-based spin FET, in which carriers are injected into a Si channel FET from ferromagnetic GaMnP. The GaP is almost lattice-matched to Si.

Among photonic devices the simplest seems to be the concept of a light emitting diode (LED) with one of the contact layers made ferromagnetic by incorporation of transition metal impurities, a so-called spin LED [77–79]. Such a device should allow us to modulate the polarization of the light emitted by the spin LED by application of an external magnetic field. The most straightforward approach to achieve this goal would be to implant Mn into the top contact p-GaN layer of the standard GaN/InGaN LED. The electrical and luminescent properties of such devices show that they do produce electroluminescence but, due to the difficulty in annealing out all radiation defects, the series resistance and the turn-on voltage of such spin LEDs are very much higher than for ordinary LEDs and the electroluminescence
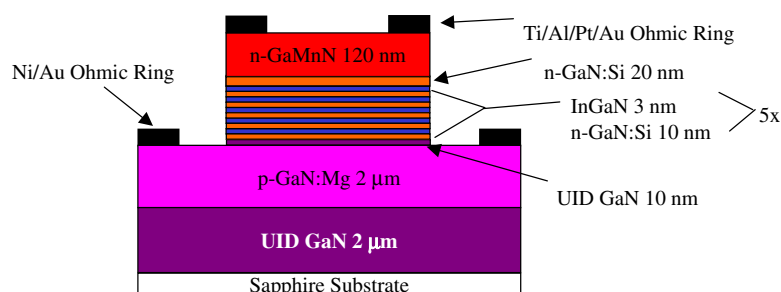
Figure 26. Schematic of LED structure.

intensity EL is lower. GaMnN layers produced by MBE have a lower density of defects and may be better suited for spin LEDs. One of the problems with the latter approach is that the MBE-grown GaMnN films with high Curie temperature have n-type conductivity. Therefore, to incorporate such layers into the GaN-based LEDs one has to reverse the usual order of layers and grow a LED structure with the contact n-layer up. It was shown that problems, such as higher series resistance due to lower lateral conductivity of p-GaN compared to n-GaN, are inherent to these inverted diodes. Also it was shown that it is more difficult to attain a high quality of the GaN/InGaN multi-quantum-well active region when growing it on top of a very heavily Mg-doped p-GaN layer. Incorporation of Mn into the top contact layer also produced a relatively high resistivity of the GaMnN and a poorer quality of the ohmic contact. In addition, the ferromagnetism in GaMnN is found to be unstable against the type of high temperature (900 °C) anneals used to minimize contact resistance.

The reference n-LED structure studied by our group consisted of 2 μm-thick undoped semi-insulating GaN, 2 μm-thick p-GaN(Mg), five undoped QWs of InGaN ($\sim$40% In, 3 nm), separated by Si-doped n-GaN barriers (10 nm each) and about a 170 nm-thick top n-GaN contact layer. All the layers but the top n-GaN layer were grown by MOCVD in a regime similar to the one used to fabricate standard p-LED structures. The n-type layer was grown by MBE at 700 °C.

The spin LED structure differed from the n-LED structure by the structure of the top n-layer which consisted of 20 nm of n-GaN(Si) and 150 nm of GaMnN with the Mn concentration close to 3%. The GaMnN layer was grown at 700 °C. All structures were subjected to a rapid thermal anneal in nitrogen to activate the Mg acceptors. However, the spin LED structure was given only a 750 °C anneal since the degree of magnetic ordering in the GaMnN MBE-grown layer was greatly reduced upon annealing at temperatures exceeding 800 °C. A schematic of the LED structure is shown in figure 26.

Measurable room temperature electroluminescence which peaked at $\sim$450 nm was detected at 4 V bias in the reference diode and at $\sim$15 V in the spin LED structure processed at 750 °C—figure 27. However, in spite of the ferromagnetic behaviour of the (Ga, Mn)N layer, no polarization of light emission at room temperature was observed in applied magnetic fields ranging from 0 to 5 T during either EL or PL measurements, as shown in figure 28 where the spin LED structure with a 100 nm-thick (Ga, Mn)N layer is taken as an example. This can be attributed either to severe spin losses in the structure during spin injection or to a poor performance of the (Ga, Mn)N layer as a spin aligner at room temperature.

Possible origins of the vanishing spin injection efficiency of the spin LED at room temperature can be clarified by analysing its properties at low temperatures which should improve magnetic performance of the DMS layer. Such an analysis was performed by utilizing
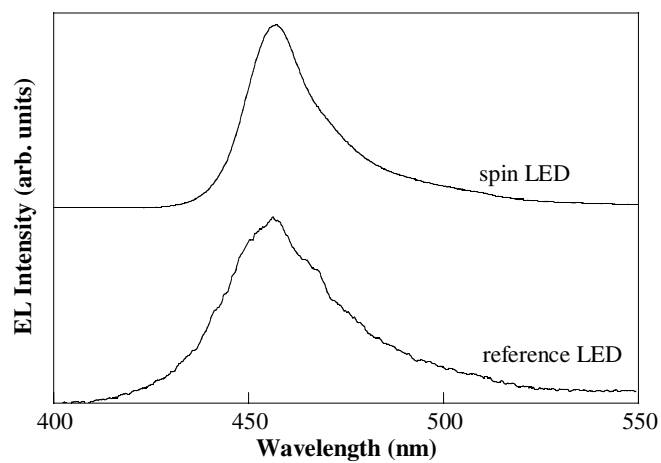
Figure 27. Typical EL spectra measured at room temperature from the Mn-doped LED annealed at 750 °C and reference diode.
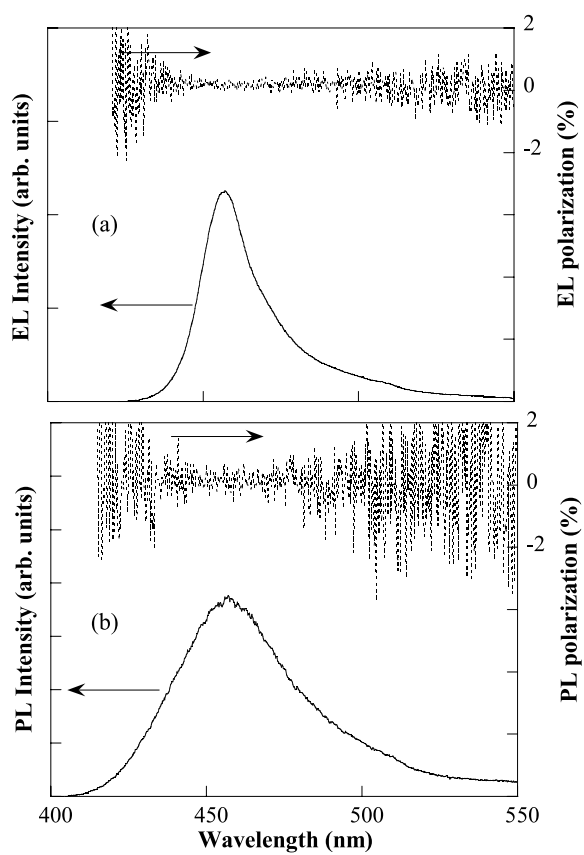

Figure 28. Comparison of the EL (a) and PL (b) spectra measured at room temperature from the same spin LED structure, as well as their polarization properties at 5 T (the upper part of each figure).
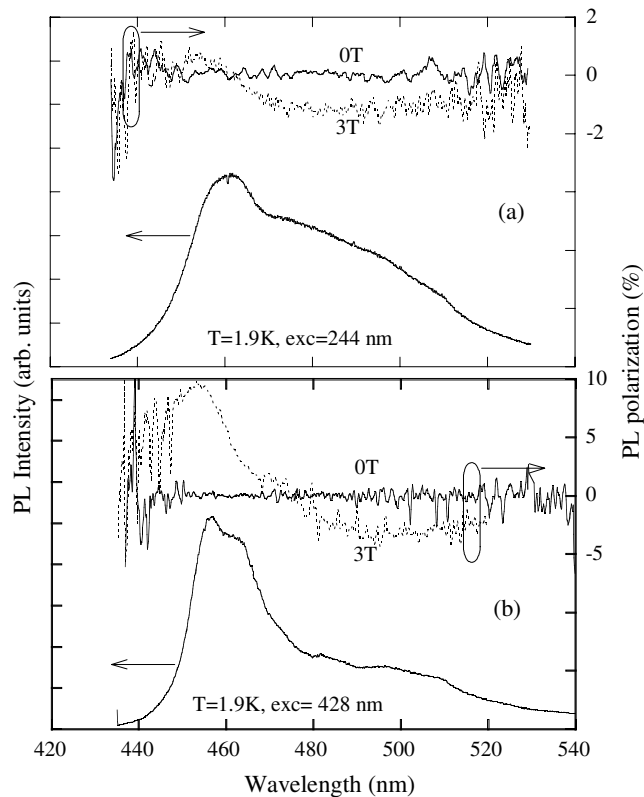
Figure 29. PL spectra at 1.9 K from the (Ga, Mn)N/InGaN diode, using optical injection from the (Ga, Mn)N layer (a) and direct optical excitation of the MQW (b). The upper part of each figure shows PL polarization at 0 T (full curves) and 3 T (broken curves).

PL measurements, since the freeze-out of free carriers at low temperatures prevented us from observation of efficient EL in the investigated structures. The spin injection efficiency was evaluated using the excitation photon energy of about 5 eV, i.e. well above the bandgap of the top (Ga, Mn)N layer. Under these conditions the preferential light absorption within the top (Ga, Mn)N layer should ensure that the dominant portion of the carriers and excitons participating in the radiative recombination in the InGaN QW is supplied by the magnetic barrier. The results of the performed measurements are summarized in figure 29 (top). The optical (spin) polarization of the QW PL was only detected in an applied magnetic field and was generally very weak (<2%). The observed PL polarization reflects combined effects of the spin injection from the magnetic (Ga, Mn) M layer and intrinsic polarization of the InGaN QW. The latter has separately been studied by tuning the excitation energy below the bandgap of GaN (also presumably GaMnN), i.e. by resonant optical excitation of the InGaN QW with a photon energy of 2.9 eV—figure 29 (bottom). It gives up to 5–10% at 2 K with an applied magnetic field of up to 5 T, most likely due to population distribution between spin sublevels at a low temperature. This value is consistent with that obtained in the reference samples.

As is obvious from figure 29, polarization properties of the InGaN QW with and without carrier supply from the magnetic layer seem to be very similar except for a consistent reduction of optical polarization of the InGaN QW upon optical excitation of GaMnN, detected for all investigated structures. One could speculate that this might be caused by injection of the
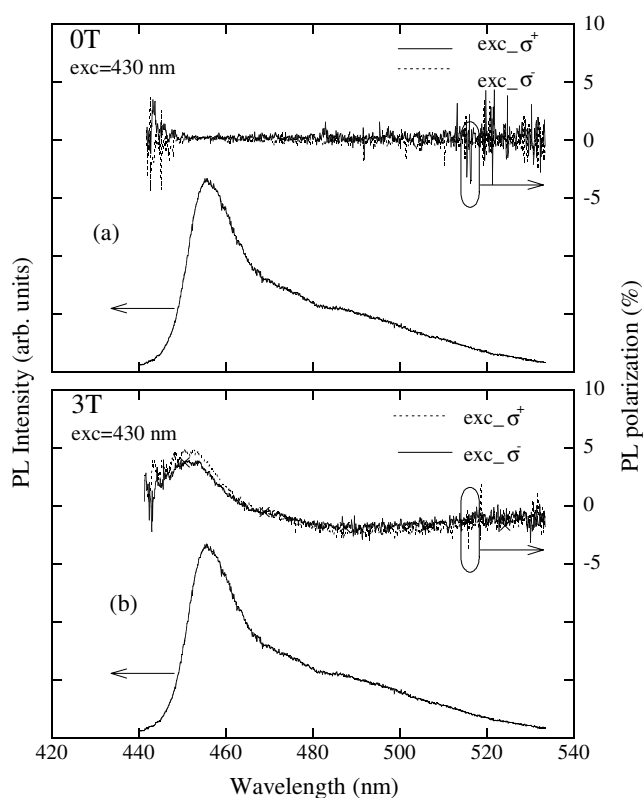
Figure 30. PL intensity and polarization at 1.9 K from the (Ga, Mn)N/InGaN diode obtained under optical excitation with the circularly polarized light specified in the figure, obtained at 0 T (a) and 3 T (b).

electrons with spin orientation opposite to that of the lowest spin state in the InGaN QW. As the degree of polarization is very low, a definite conclusion on this issue cannot be obtained and requires further investigation.

In order to shed light on the possible origin for the weak spin polarization of the InGaN QW, optical orientation experiments were performed where a chosen spin orientation of excitons/carriers in the InGaN QW was generated by the relevant circularly polarized excitation light resonantly pumping the InGaN QW. No spin polarization was observed at 0 T (figure 30), showing that the generated spin orientation was completely lost during the energy relaxation process to the ground state of the excitons giving rise to the PL. This is in sharp contrast to the cases in II–VI and GaAs, where spin polarization can usually be observed in such optical orientation experiments. With an applied magnetic field, the spin polarization of the InGaN QW is independent of the polarization of the excitation light which again proves that the spin relaxation in the InGaN QW is extremely efficient. The exact physical mechanism responsible for this fast spin relaxation is currently unknown and requires in-depth experimental and theoretical studies.

These findings imply the fast spin relaxation within the InGaN QW is enough to destroy any injected spin polarization leading to the observed low spin injection efficiency in the studied (Ga, Mn)N/GaInN spin LEDs. This therefore calls for further in-depth studies of spin relaxation processes in GaN-based materials and quantum structures aiming at optimization of spin detectors as a necessary step in understanding spin injection processes and also in improving

Table 1. Compilation of semiconductors showing room temperature ferromagnetism.

Material	Bandgap of host (eV)	Comments	Ordering temperature (K)	References
$Cd_{1-x}Mn_xGeP_2$	1.72	Solid-phase reaction of evaporated Mn	>300	[7]
(Ga, Mn)N	3.4	Mn incorporated by diffusion	228–370	[22]
(Ga, Mn)N	3.4	Mn incorporated during MBE; n-type	>300	[29]
(Ga, Mn)N	3.4	Mn incorporated during MBE	940[a]	[25]
(Ga, Cr)N	3.4	Cr incorporated during MBE or bulk growth	>400	[34]
(ZnO):Co	3.1–3.6	Co incorporated during PLD; ~15% Co	>300	[9]
(ZnO):Co	3.3	Sintered powders	>425	[82]
(Al, Cr)N	6.2	Cr incorporated during MBE, sputtering or implantation	>300	[52, 53, 81]
(Ga, Mn) P:C	2.2	Mn incorporated by implant or MBE; $p \sim 10^{20}$ cm^{-3}	>330	[68]
$(Zn_{1-x}Mn_x)GeP_2$	1.83–2.8	Sealed ampoule growth; insulating; 5.6% Mn	312	[6]
(ZnMn) GeP$_2$	<2.8	Mn incorporated by diffusion	350	[7]
ZnSnAs$_2$	0.65	Bulk growth	329	[8]
ZnSiGeN$_2$	3.52	Mn-implanted epi	~300	[80]
SiC	3.2	Mn or Fe implantation	~300 (by hysteresis)	[31, 32]

[a] Extrapolated from measurements up to ~750 K.

performance of possible spintronic devices based on III-nitrides. Table 1 summarizes recent reports of room temperature ferromagnetism in semiconductors.

12. Issues to be resolved

The mean-field models consider the ferromagnetism to be mediated by delocalized or weakly localized holes in the p-type materials. The magnetic Mn ion provides a localized spin and acts as an acceptor in most III–V semiconductors so that it can also provide holes. In these models, the T_C is proportional to the density of Mn ions and the hole density. Many aspects of the experimental data can be explained by the basic mean-field model. However, ferromagnetism has been observed in samples that have very low hole concentrations, in insulating material and, more recently, in n-type material.

More work is also needed to establish the energy levels of the Mn, whether there are more effective magnetic dopant atoms and how the magnetic properties are influenced by carrier density and type [83]. Even basic measurements, such as how the magnetism changes with carrier density or type and how the bandgap changes with Mn concentration in GaN, have not been performed. There is a strong need for a practical device demonstration showing spin functionality in a nitride-based structure, such as spin LED or tunnelling magnetoresistance device. The control of spin injection and manipulation of spin transport by external means, such as voltage from a gate contact or magnetic fields from adjacent current lines or ferromagnetic contacts, is at the heart of whether spintronics can be exploited in device structures and these areas are still in their infancy.

Acknowledgments

References

[1] See, for example, von Molnar S and Read D 2003 *Proc. IEEE* **91** 715
    Dietl T 2002 *Semicond. Sci. Technol.* **17** 377
    Ohno H 2000 *J. Vac. Sci. Technol.* B **18** 2039
[2] Wolf S A, Awschalom D D, Buhrman R A, Daughton J M, von Molnar S, Roukes M L, Chtchelkanova A Y and Treger D M 2001 *Science* **294** 1488
[3] Ohno H, Matsukura F and Ohno Y 2002 *JSAP Int.* **5** 4
[4] Awschalom D D and Kikkawa J M 2000 *Science* **287** 473
[5] Cho S *et al* 2002 *Phys. Rev. Lett.* **88** 257203-1
[6] Medvedkin G A, Ishibashi T, Nishi T and Hiyata K 2000 *Japan. J. Appl. Phys.* **39** L949
[7] Medvedkin G A, Hirose K, Ishibashi T, Nishi T, Voevodin V G and Sato K 2002 *J. Cryst. Growth* **236** 609
[8] Choi S, Cha G B, Hong S C, Cho S, Kim Y, Ketterson J B, Jeong S-Y and Yi G C 2002 *Solid State Commun.* **122** 165
[9] Ueda K, Tahata H and Kawai T 2001 *Appl. Phys. Lett.* **79** 988
[10] Chambers S A 2002 *Mater. Today* (April) 34–9
[11] Dietl T, Ohno H, Matsukura F, Cibert J and Ferrand D 2000 *Science* **287** 1019
[12] Van Schilfgaarde M and Myrasov O N 2001 *Phys. Rev.* B **63** 233205
[13] Dietl T, Ohno H and Matsukura F 2001 *Phys. Rev.* B **63** 195205
[14] Dietl T 2001 *J. Appl. Phys.* **89** 7437
[15] Jungwirth T, Atkinson W A, Lee B and MacDonald A H 1999 *Phys. Rev.* B **59** 9818
[16] Berciu M and Bhatt R N 2001 *Phys. Rev. Lett.* **87** 108203
[17] Bhatt R N, Berciu M, Kennett M D and Wan X 2002 *J. Supercond. Incorp. Novel Magn.* **15** 71
[18] Litvinov V I and Dugaev V A 2001 *Phys. Rev. Lett.* **86** 5593
[19] Konig J, Lin H H and MacDonald A H 2001 *Phys. Rev. Lett.* **84** 5628
[20] Schliemann J, Konig J and MacDonald A H 2001 *Phys. Rev.* B **64** 165201
[21] Reed M L, Ritums M K, Stadelmaier H H, Reed M J, Parker C A, Bedair S M and El-Masry N A 2001 *Mater. Lett.* **51** 500
[22] Reed M L, Ritums M K, Stadelmaier H H, Reed M J, Parker C A, Bedair S M and El-Masry N A 2001 *Appl. Phys. Lett.* **79** 3473
[23] Theodoropoulou N, Hebard A F, Overberg M E, Abernathy C R, Pearton S J, Chu S N G and Wilson R G 2001 *Appl. Phys. Lett.* **78** 3475
[24] Overberg M E, Abernathy C R, Pearton S J, Theodoropoulou N A, McCarthy K T and Hebard A F 2001 *Appl. Phys. Lett.* **79** 1312
[25] Sonoda S, Shimizu S, Sasaki T, Yamamoto Y and Hori H 2002 *J. Cryst. Growth* **237–239** 1358
[26] Kim K H, Lee K J, Kim D J, Kim H J, Ihm Y E, Djayaprawira D, Takahashi M, Kim C S, Kim C G and You S H 2003 *Appl. Phys. Lett.* **82** 1775
[27] Soo Y L, Kioseoglou G, Kim S, Huang S, Koo Y H, Kuwarbara S, Owa S, Kondo T and Munekata H 2001 *Appl. Phys. Lett.* **79** 3926
[28] Kuwabara S, Kondo T, Chikyou T, Ahmet P and Munekata H 2001 *Japan. J. Appl. Phys.* **40** L724
[29] Thaler G T *et al* 2002 *Appl. Phys. Lett.* **80** 3964
[30] Hori Sonoda S, Sasaki T, Yamamoto Y, Shimizu S, Suga K and Kindo K 2002 *Physica* B **324** 142
[31] Pearton S J, Abernathy C R, Norton D P, Hebard A F, Park Y D, Boatner L A and Budai J D 2003 *Mater. Sci. Eng.* R **40** 137
[32] Pearton S J, Abernathy C R, Overberg M E, Theodoropoulou N, Hebard A F, Park Y D, Ren F, Kim J and Boatner L A 2003 *J. Appl. Phys.* **93** 1

[33] Dhar S, Brandt O, Trampert V, Daweritz A L, Friedland K J, Ploog K H, Keller J, Beschoten B and
    Guntherhold G 2003 *Appl. Phys. Lett.* **82** 2077

[34] Park M C, Huh K S, Hyong J M, Lee J M, Chung J Y, Lee K I, Han S H and Lee W Y 2002 *Solid State Commun.*
    124 11

[35] Lee J S, Lim J D, Khim Z G, Park Y D, Pearton S J and Chu S N G 2003 *J. Appl. Phys.* **93** 4512

[36] Ando K 2003 *Appl. Phys. Lett.* **82** 100

[37] Baik J M, Kim J K, Yang H W, Shon Y, Kang T W and Lee J L 2002 *Phys. Status Solidi* b **234** 943

[38] Sardar K, Raju A R, Basal B, Venkataraman V and Rao C N R 2003 *Solid State Commun.* **125** 55

[39] Baik J M, Yang H W, Kim J K and Lee J-L 2003 *Appl. Phys. Lett.* **82** 583

[40] Shon Y, Kwon H, Yuldashev Sh U, Park Y S, Fu D J, Kim D Y, Kim H S and Kang T W 2003 *J. Appl. Phys.*
    93 1546

[41] Dietl T, Ohno H and Matsukura F 2001 *Phys. Rev.* B **63** 195205

[42] Dugaev V K, Litvinov V I, Barnes J and Viera M 2003 *Phys. Rev.* B **67** 033201

[43] Schliemann J 2003 *Phys. Rev.* B **67** 045202

[44] Rao B K and Jena P 2002 *Phys. Rev. Lett.* **89** 185504

[45] Korotkov R Y, Gregie J M and Wessels B W 2002 *Appl. Phys. Lett.* **80** 1731

[46] Graf T, Gjukic M, Brandt M S, Stutzmann M and Ambacher O 2002 *Appl. Phys. Lett.* **81** 5159

[47] Polyakov A Y *et al* 2002 *J. Appl. Phys.* **92** 4989

[48] Theodoropoulou N A, Hebard A F, Chu S N G, Overberg M E, Abernathy C R, Pearton S J, Wilson R G and
    Zavada J M 2001 *Appl. Phys. Lett.* **79** 3452

[49] Pearton S J *et al* 2002 *J. Vac. Sci. Technol.* A **20** 583

[50] Akinaga H, Nemeth S, De Boeck J, Nistor L, Bender H, Borghs G, Ofuchi H and Oshima M 2000 *Appl. Phys.
    Lett.* **77** 4377

[51] Hashimoto M, Zhou Y Z, Kanamura M and Asahi H 2002 *Solid State Commun.* **122** 37

[52] Yang S G, Pakhomov A B, Hung S T and Wong C Y 2002 *Appl. Phys. Lett.* **81** 2418

[53] Wu S Y, Liu H X, Gu L, Singh R K, Budd L, Schilfgaaarde M, McCartney M R, Smith D J and Newman N 2003
    Appl. Phys. Lett. **83** 3255

[54] Liu C, Alves E, Ramos A R, da Silva M F, Soares J C, Matsutani T and Kiuchi M 2002 *Nucl. Instrum. Methods
    Phys. Res.* B **191** 544

[55] Ohno H, Shen S, Matsukura F, Oiwa A, Endo A, Katsumoto S and Iye Y 1996 *Appl. Phys. Lett.* **69** 363

[56] Janotti L, Wei S and Bellaiche L 2003 *Appl. Phys. Lett.* **82** 766

[57] Martin A L, Spalding C M, Dimitrova E I, Van Patten P G, Caldwell M C, Kordesch M E and Richardson H H
    2001 *J. Vac. Sci. Technol.* A **19** 1894

[58] Lu F, Carius R A, Alam Heuken M and Buchal Ch 2002 *J. Appl. Phys.* **92** 2457

[59] Cho D-H, Shimizu M, Ide T, Ookita H and Koumwa H 2002 *Japan. J. Appl. Phys.* **41** 4481

[60] Hu X, Deng J, Pala N, Gaska R, Shur M S, Chen C Q, Yang J, Simin G, Khan M A, Rojo J C and Schwalker Z J 2003
    Appl. Phys. Lett. **82** 1299

[61] Serina F, Ng K Y S, Huang C, Amer G W, Romni L and Naik R 2001 *Appl. Phys. Lett.* **79** 3350

[62] Lee S H, Lee J K and Yoon K H 2003 *J. Vac. Sci. Technol.* A **21** 1

[63] Takagaki Y, Santos P, Wiebicke E, Brandt O, Schmerr J D and Ploog K 2002 *Appl. Phys. Lett.* **81** 2538

[64] Kipshidze G, Kuryatkov V, Zhu K, Vorizov B, Holtz M, Nikishin S and Temkin H 2003 *J. Appl. Phys.* **93** 1363

[65] Nishida T, Kobayashi N and Ban T 2003 *Appl. Phys. Lett.* **82** 1

[66] Gaska R, Chen C, Yang J, Kookstis E, Kahn M A, Tamulaitis G, Yilmog I, Shur M S, Rojo J C and
    Schowalter L J 2002 *Appl. Phys. Lett.* **81** 4658

[67] Yang S G, Pakhomov A B, Hung C Y and Wong C Y 2002 *Appl. Phys. Lett.* **81** 2418

[68] Theodoropoulou N, Hebard A F, Overberg M E, Abernathy C R, Pearton S J, Chu S N G and Wilson R G 2003
    Phys. Rev. Lett. **89** 107203

[69] Kucheyev S O, Williams J S, Zou J, Jagadish C, Pophristic M, Guo S, Ferguson I T and Manasreh M O 2002
    J. Appl. Phys. **92** 3554

[70] Li J, Nam K B, Nakarmi M C, Lin J Y and Jiang H X 2002 *Appl. Phys. Lett.* **81** 3365

[71] Hashimoto M, Zhou Y-K, Kanamura M and Asahi H 2002 *Solid State Commun.* **122** 37

[72] Nam K B, Li J, Kim K H, Lin K H and Jiang H X 2001 *Appl. Phys. Lett.* **78** 3690

[73] Ji Y, Stijkers G J, Yang F Y, Chien C C, Byers J M, Angvelovch A, Xiao G and Gupta A 2001 *Phys. Rev. Lett.*
    86 5585

[74] Inumarn K, Okamoto H and Yamanka S J 2002 *J. Cryst. Growth* **237–239** 2050

[75] Suzuki K, Kancho T, Yoshida H, Morita H and Fujimori H 1995 *J. Alloys Compounds* **224** 232

[76] Ohno Y, Young D K, Beschoten B, Matsukura F, Ohno H and Awschalom D D 1999 *Nature* **402** 790

[77] Jonker B T, Park Y D, Bennet B R, Cheong H D, Kioseoglou G and Petrou A 2000 *Phys. Rev.* B **62** 8180

[78] Park Y D, Jonker B T, Bennet B R, Itzkos G, Furis M, Kioseoglou G and Petrou A 2000 *Appl. Phys. Lett.* **77** 3989

[79] Jonker B T, Hanbicki A T, Park Y D, Itskos G, Furis M, Kioseoglou G and Petrou A 2001 *Appl. Phys. Lett.* **79** 3098

[80] Pearton S J *et al* 2002 *J. Appl. Phys.* **92** 2047

[81] Frazier R M, Thaler G, Abernathy C R and Pearton S J 2003 *Appl. Phys. Lett.* **83** 1758

[82] Sharma P, Gupta A, Rao K V, Owens F J, Sharma R, Ahuja R, Osorio Guillen J M, Johansson B and Gehring G A 2003 *Nature* **2** 673

[83] Graf T, Goennenwein S T B and Brandt M S 2003 *Phys. Status Solidi* b **239** 277